# On the spectral wave climate of the French Atlantic Ocean

Sartini, Ludovica; Antonini, Alessandro

**DOI**
10.1016/j.oceaneng.2024.117900

**Publication date**
2024

**Document Version**
Final published version

**Published in**
Ocean Engineering

Ocean Engineering 304 (2024) 117900

Contents lists available at ScienceDirect

Ocean Engineering

journal homepage: www.elsevier.com/locate/oceaneng

# On the spectral wave climate of the French Atlantic Ocean

Ludovica Sartini [a,b,*], Alessandro Antonini [c]

[a] RINA Consulting S.p.A, MetOcean Unit, 16129, Genoa, Italy

[b] IFREMER, Recherches et Développements Technologiques Unité, Laboratoire Comportement des Structures en Mer (PDG-REM-RDT-LCSM), 29280, Plouzane, France

[c] Department of Hydraulic Engineering, Delft University of Technology, The Netherlands

ARTICLE INFO

*Keywords:*
Wave climate
Wave spectra
Wave systems
Spectral partitioning

ABSTRACT

The accurate description of wave climate at different spatio-temporal scales requires the application of advanced statistical models together with a good knowledge of geophysical processes. Furthermore, accurate modelling of multimodal sea states is of primary importance for most of offshore and coastal activities, such as wave energy device optimization, maritime design practice and for safety at sea. The present manuscript is conceived within this scientific framework proposing to assess wave climate of a complex area of French Atlantic Ocean bordering seas. The main "Spectral Climatology Types" of the area are identified as resulting of defined combinations of wave systems detected through directional spectra and partitioned wave systems analysis. The presence of swell systems is evaluated quantitatively on the whole area, characterized by different regimes of multimodal sea-states at strong regional variability and put into relation with main meteorological forcing active on the area at different spatial scales. Celtic Sea exhibits a marked regional characterization with a prevalence of multimodal conditions given by different combination of wave systems with increasing contribution of swell systems moving from North-West to South. A significant presence of crossing sea states is observed in South Celtic Sea especially in proximity of bathymetric slope. The South Bay of Biscay is influenced by fully developed swell systems enhanced by refraction effects caused by both the coastline and bathymetry gradients. English Channel and North Sea show complex sea-states conditions induced by local topography features together with wind channelling and tide effects able to trigger geophysical processes at a sub-scale responsible for the development of multimodal seas. Crossing and bimodal seas are also found to be influenced by bathymetry gradients acting directly on the directional spectrum shape as well as by tide due to tidal current-induced refraction effect on wave propagation. No generalized significant trends are detected within the investigated spatial domain for the wave spectrum integral quantities; locations sited at northern Celtic Sea show a downward Significant Wave Height, while only locations confined at eastern English Chanel only shows a Peak Period upward trend.

## 1. Introduction

A proper definition of sea states and wave climate is of primary importance to carry out a wide range of marine activities such as offshore and coastal structures design and assessment (Espejo et al., 2014; Antonini et al., 2017; Anon, 2019; Raby et al., 2019), marine energy exploitation (Anon, 2021a,b), shipping and forecasting (Scipione et al., 2024; Ewans et al., 2004; Jonathan et al., 2008), as well for coastal management as they play a key role on coastal erosion (Ardhuin et al., 2009; Sanil Kumar et al., 2011; Polidoro et al., 2018). A thorough knowledge of wave energy assessment and how it is allocated within the coexisting wave systems can serve as the optimal framework to support the extreme boundary conditions assessment of homogeneous data. In particular, separation and identification of sea state conditions as the superimposition of local wind seas and swell events propagation over long distances provide a real asset to the performance of said activities, (Portilla-Yandún et al., 2016; Portilla-Yandún, 2018). As a result, wave climate assessment on complex domains constitutes a complicated framework especially when different spatio-temporal scales overlap. This is even more challenging when the presence of coastal processes adds up to wave dynamics active on a larger scale, together with effects performed by peculiar bathymetry features and coastal morphology.

A robust description of wave climate should be supported by a thorough analysis of actual wave energy spectral distribution within co-existing sea-states, especially in areas wherein complex sea-states are of relevance. Directional wave spectra showing wave energy distribution as a function of frequencies and direction usually exhibit a structure

* Corresponding author at: RINA Consulting S.p.A, MetOcean Unit, 16129, Genoa, Italy.
*E-mail address:* ludovica.sartini@rina.org (L. Sartini).

https://doi.org/10.1016/j.oceaneng.2024.117900
Received 10 October 2023; Received in revised form 11 April 2024; Accepted 13 April 2024
Available online 22 April 2024

which represents local wave systems. On the other hand, directional spectra are not easy to be accessed, managed and stored. Furthermore, swell heights are relatively poorly predicted since their energy should be weakly dissipated, even if a suitable wave model parameterization (ST4) has been developed just to tackle the issue (Ardhuin et al., 2009).

Dynamical spectral partitioning represents a valid technique for the identification of different wave systems. In the last decade, different partitioning techniques were implemented for wave systems identification (Gerling, 1992; Hasselmann et al., 1996; Hanson and Phillips, 1999, 2001). More recently, Ailliot et al. (2013) proposed a new method for partitioning directional wave spectra based on a sequential Monte Carlo algorithm validated against both synthetic and modelled time series of spectra. Similarly, a new approach for identifying coherent temporal sequences of spectral components based on the Watershed algorithm (Gerling, 1992; Hasselmann et al., 1996) applied to field data is presented in Kpogo-Nuwoklo et al. (2015), while the WaveSEP (Wave Spectrum Energy Partitioning) method is also noteworthy (Tracy et al., 2007; Devaliere et al., 2009). Chen et al. 2015 proposed a practical method based on the overshoot phenomenon for extracting wind sea and swell events from directional spectra (Chen et al., 2015).

Since multimodal spectra are associated with wave systems generated by different meteorological events, it can be deduced that different wave climates may arise from complex sea states assigned to different wave systems. In this regard, the proper characterization of directional spectra and wave partitions can be conceived as valid support for wave climate definition. For instance, in Olagnon et al. 2014 a spatial processing of directional spectra for the definition of long-term statistics of the swell climate of West Africa is performed, (Olagnon et al., 2014).

The present manuscript moves into the framework of high resolution spectral partitioning analysis for wave climate assessment to define the main "Spectral Climatology Types" of French Atlantic Ocean, especially within the Bay of Biscay and the English Channel, as the area exhibits a complex distribution of wave spectral energy, responsible for the superimposition of wind sea and swell for about two-thirds of total sea states (Maisondieu and Le Boulluec, 2016).

Similar to Portilla et al. (2016) (Portilla-Yandún et al., 2016), our study delves into the main wave climate patterns of the region through a wave spectra partitioning assessment. However, the unique spatial high resolution of the HOMERE model (down to 100 m in the coastal areas) allows us to investigate finer-scale dynamics that could not be captured by the pioneering work proposed by Portilla-Yandún (2018) (Portilla-Yandún, 2018) due to the coarser grid (around 100 km) of the ERA-Interim reanalysis data.

In this regard, 23 years of partitioned wave hindcast data at high spatial resolution are used to evaluate the occurrences of wave systems defining the complex sea-states system characterizing the area of study.

The meteorological counterpart responsible for the generation of various wave systems on different source regions is also investigated, together with the influence of other geophysical processes (such as tide or bathymetry) on their final spatial assessment. Upon completion, the presence of any long-term trend within the integral Significant Wave Height ($H_S$) and Peak Period ($T_P$) is also investigated to evaluate the effects of climate changes on spatial wave climate. In brief, the objective of this work is threefold:

- to enrich the literature focused on the wave climate of the French Atlantic Ocean due to its complexity and importance for several maritime activities;
- to leverage the availability of partitioned wave hindcast data within the scientific community as a tribute to scientific commitment;
- to perform a "High resolution Spatial Spectral Climatology" definition of the whole area, never done before.

The manuscript is organized as follows: wave model and directional spectra used in the analysis are described in Sections 2.1 and 2.2. Findings related to the spectra analysis and wave climate patterns are discussed in Section 3, while the conclusions are provided in Section 4.

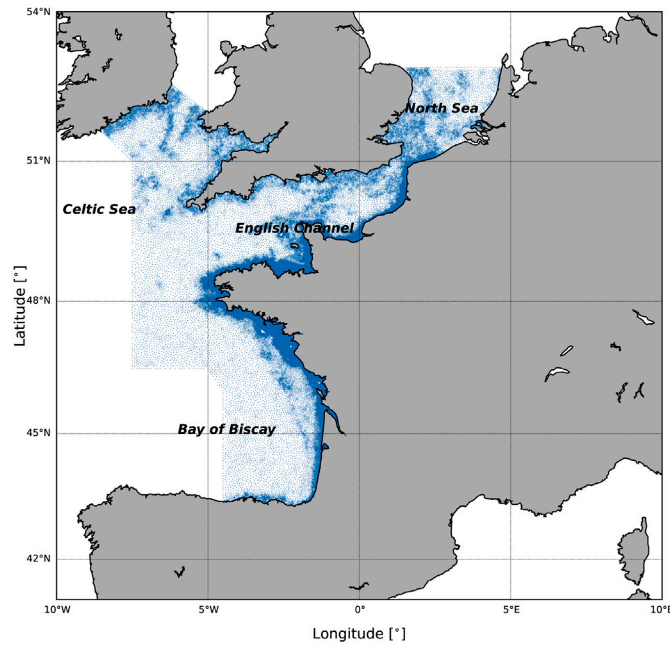


**Fig. 1.** Domain of HOMERE database.

## 2. Methods

### 2.1. Wave model and hindcast data

Wave data used for this study are extracted from the sea-states hindcast database HOMERE, described in Boudière et al. (2013). Data were generated through WAVEWATCH III model (version 4.11) running over an unstructured mesh at high-resolution (~110 000 points), ranging from 10 km to 200 m, adapted at various scales from the open sea to the shore, and covering a 23-years from 1994 to 2016. The model domain spans the Atlantic Ocean along the southern coast of Ireland, encompassing the Celtic Sea, the English Channel, and a portion of the North Sea. Fig. 1 shows the detailed extension of the irregular grid domain. The over 110.000 blue dots in Fig. 1 represent the model grid nodes (i.e. where the model outputs are available in terms of time series), the grey areas depict the land and are bounded by the thick solid black lines representing the coastline, while the thin solid lines highlight the geographical coordinates for the investigated area. The white areas are not considered within the model and they are shown merely for the sake of map completeness. The model captures coastline reflection through a parameterization that includes a variable reflection coefficient. This coefficient is determined by factors such as the shoreface slope, shoreline geomorphology, and wave characteristics, including incident wave height and mean frequency. The approach proves effective in minimizing errors in mean directional spreading, particularly in regions where the precise estimation of the shoreface slope is feasible, as outlined by Arduin and Aron in 2012 (Ardhuin and Roland, 2012). The computed spectra are discretized over 24 directions (i.e. each sector is 15 degrees wide) and 32 frequencies (ranging from 0.0373 to 0.7159 Hz). The model is forced by CFSR (Climate Forecast System Reanalysis) wind fields reanalysis (Saha et al., 2010) at a spatial resolution of about 0.5°. Water levels, surges and currents are provided by 2D shallow water equations MARS hydrodynamic model (Lazure and Dumas, 2008). To consistently reproduce sea states on the domain, the model is forced at the open boundaries with the directional spectra derived from simulations of the global model of The Integrated Ocean Waves for Geophysical and other Applications (IOWAGA), updated every hour.

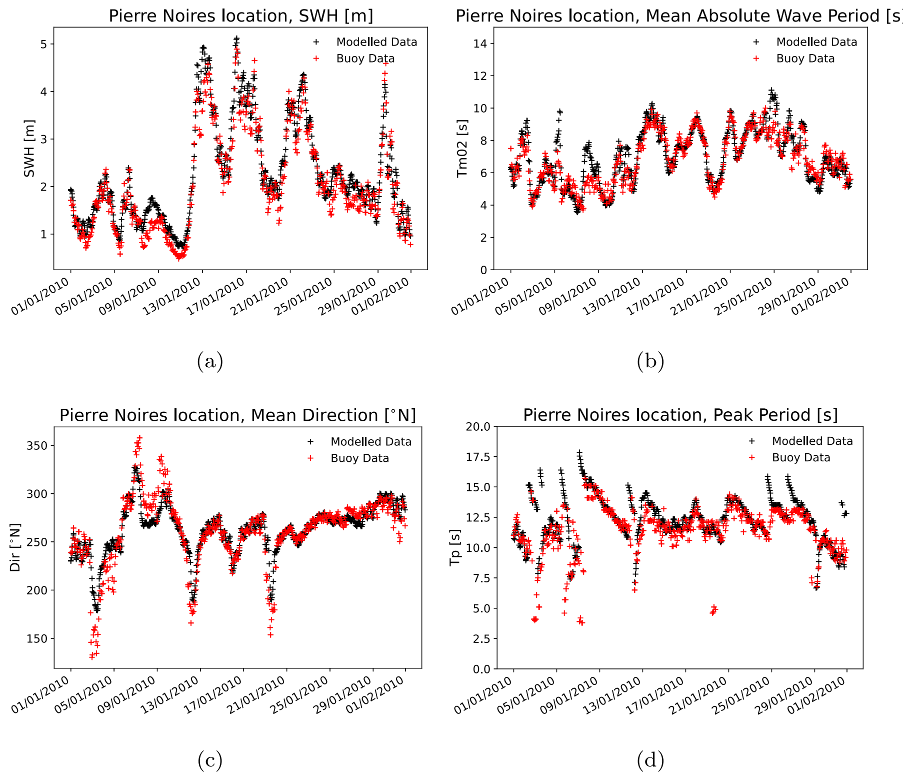


**Fig. 2.** Comparison between modelled and observed wave data ($H_s$, Mean Period $Tm02$, Mean Direction $Dir$ and Peak Period $T_p$) at Pierre Noires location, Brittany. In red: measured data, and in black: simulated data.

A comprehensive array of global parameters, including significant wave height, peak period, and mean direction, is recorded at each grid point with an hourly time step. Additionally, parameters of specific relevance to ocean engineering and marine applications, such as wave energy flux, surface Stokes drift, and radiation stresses, are also saved. Furthermore, directional spectra are accessible at over 4000 points, all with the same temporal resolution. For an in-depth understanding of the numerical model setup, detailed information is offered by Boudière et al. (2013). The validation of the model was thoroughly examined, utilizing in-situ measurements from directional buoys and remote sensing data from satellite altimeters. Additionally, a comparative analysis was conducted with NOAA's WWIII model output for both wave and wind values, as documented by Boudière et al. (2013). Although the model had previously undergone extensive validation, this study presents additional findings to ensure comprehensive model reliability in coastal areas. Fig. 2 shows the comparison between modelled and measured, as extracted from the Pierre Noires coastal buoy (Lat: 48.290°, Lon: −4.968.31°), wave parameters time series ($H_s$, Mean Period $Tm02$, Mean Direction $Dir$ and Peak Period $T_p$).

The results demonstrate the numerical model's proficiency in accurately reproducing all integrated wave parameters, with minor discrepancies primarily arising from a partial mismatch between buoy locations and the extraction points of the wave model.

### 2.2. Sea-states partitioning

Global parameters associated with various wave systems (one wind sea and five swells) constituting the sea-states at each time-step are available in HOMERE database. Spectral partitioning was achieved through the WaveSEP (Wave Spectrum Energy Partitioning) partitioning method (Tracy et al., 2007; Devaliere et al., 2009) based on a digital image processing watershed algorithm (Vincent and Soille, 1991; Hanson and Jensen, 2004) able to identify energy density areas associated to different wave systems within directional spectra. These global parameters were employed to study the spatial variability of defined spectral partitions. Among these, the wind sea fraction $W$ (Komen et al., 1984) is defined as the ratio between the area in the spectral partition under the direct influence of the wind and the total spectral energy of a given partition as follows:

$$W = \frac{E|U_p|c}{E} \tag{1}$$

where the wind sea-swell separation velocity $U_p$ ($c$ represents local wave phase velocity) is quantitatively evaluated from the wave-age relationship as a function of (i) wind velocity $U_{10}$, (ii) the angular difference between wind and wave directions and (iii) wave age factor $\beta$ assumed equal to 1.7 (Hasselmann et al., 1996; Voorrips et al., 1997; Hanson and Phillips, 2001), as:

$$U_p = \beta U_{10}\left(\theta - \theta_W\right). \tag{2}$$

The parameter W allows to classify each partition as pure wind sea ($W = 1$), pure swell ($W = 0$) or mixed seas (Portilla et al., 2009). Temporal series of global wave systems parameters obtained after partitioning at a given location are reported in Fig. 3 for one month (January 1994).

In Fig. 3 an illustrative outcome of the partitioning process is presented for each wave system and for different wave parameters such as significant wave height ($hs_i$) Fig. 3(a), mean direction ($dir_i$) Fig. 3(b) and peak period ($Tp_i$) Fig. 3(c). In Fig. 3(d), wind speed and direction are presented as the primary drivers for the identified wave system and partitioning process, while in Fig. 3(e) the evolution of sea and swell is presented via the wind sea fraction coefficient $W$. Coefficient values close to 1 are mainly associated with the wind seas while a decrease to 0.38 occurs for change in wind direction as already observed by Maisondieu (2017). On the other hand, swell sea states are characterized by $W$ values close to zero with sporadic increases when wind speed decreases. The subscription $i \in [0,5]$ identifies the partitioning process results such as wind sea, the primary swell, the secondary swell, and so on. Based on the defined combinations of the

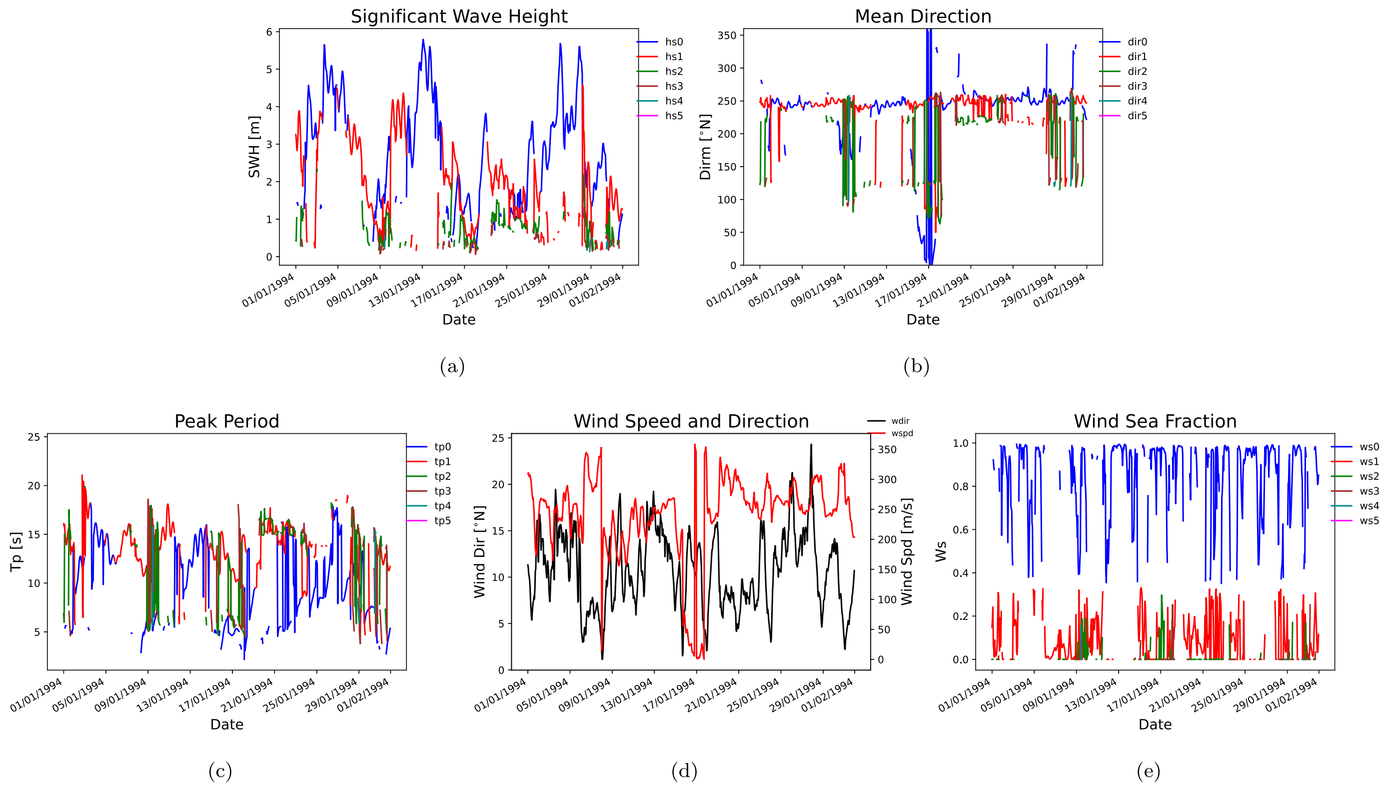


**Fig. 3.** Temporal evolution of wave systems parameters at a given location, subscription value indicates the partitioned wave system.

mentioned wave systems, the following six spectral partitioning types are identified and adopted within this work:

- SP I: wind sea only;
- SP II: swell only;
- SP III: 1 swell + 1 wind sea;
- SP IV: 2 swells only;
- SP V: 2 swell + 1 wind sea;
- SP VI: 3 swells.

More precisely, we evaluated the occurrence statistics of combinations of wave systems. This assessment involved calculating the ratio of the number of time steps during which the superimposition of wave systems was observed to the total number of time steps.

## 3. Results

### *3.1. Spatial overview*

To obtain an initial spatial overview of spectral components, we analysed all directional spectra available within the computational domain. The most intense regimes impact the western basin, particularly the Celtic Sea, and extend through the Bay of Biscay to the entrance of the English Channel. Substantial energy is also observed along the coast of the Bay of Biscay. A preliminary examination of the results reveals a spatial assessment of spectral features organized in areal patterns, resembling the discussions in Sartini et al. (2018), where a statistical division into homogeneous regions affected by the same extreme marine events was proposed. While establishing a straightforward connection between extreme events and the morphology of directional spectra may not be evident, it can be inferred that diverse meteorological forcings acting on various sub-scale areas, as detailed in Sartini et al. (2018), play a pivotal role in the occurrence of storm events and the characteristics of sea states.

The spatial distribution of occurrence statistics for each spectral partition (SPI, SPII, . . . ) reinforces the hypothesis of a zonal arrangement of sea states. Broadly, it is observed that unimodal sea states, attributed solely to wind-generated waves (Fig. 4(a)), are relatively scarce, accounting for less than 20% of the time within the Bay of Biscay. In contrast, higher occurrences are identified in the Celtic Sea and the English Channel. Specifically, the eastern English Channel and the North Sea experience increased contributions resulting from a partial obstruction of swells originating south of the UK.

Unimodal conditions solely driven by swells are consequently restricted in these areas (Fig. 4(b)). The most substantial contribution is observed in the southeast Bay of Biscay, influenced by the propagation of North-Western Atlantic events. Additionally, notable contributions are also evident along the Northern coast of Brittany and at the entrance of the English Channel, mainly due to the coastline's impact on South-Western events.

Multimodal conditions given with superimposition of wind sea and one swell are found to be more than 20% of time in the whole bay (Fig. 4(c)), with higher levels of occurrences (more than 40%) within the English Channel and the North Sea. Systems of two swells are quite limited (Fig. 4(d)), except for some coastal areas of the English Channel and the Bay of Biscay. The prevalence of sea-state conditions marked by the superimposition of one wind sea and two swells is notably low in the south-eastern sector of the Bay of Biscay. However, the occurrence percentage rises as one moves north, influenced by the refraction effect that initiates swell propagation (see Fig. 4(e)). In contrast, the emergence of a hotspot in the south-eastern corner of the Bay of Biscay underscores the focusing effect induced by the deeper canyon in the coastal bathymetry, as depicted in Fig. 5(a). The English Channel and the North Sea are characterized by a limited percentage of occurrence for this wave system, diverging from Maisondieu's observations in 2017 (Maisondieu, 2017). This dissimilarity is likely linked to the relatively low significant wave height of wave systems that do not meet the threshold for inclusion in the present analysis (Mason

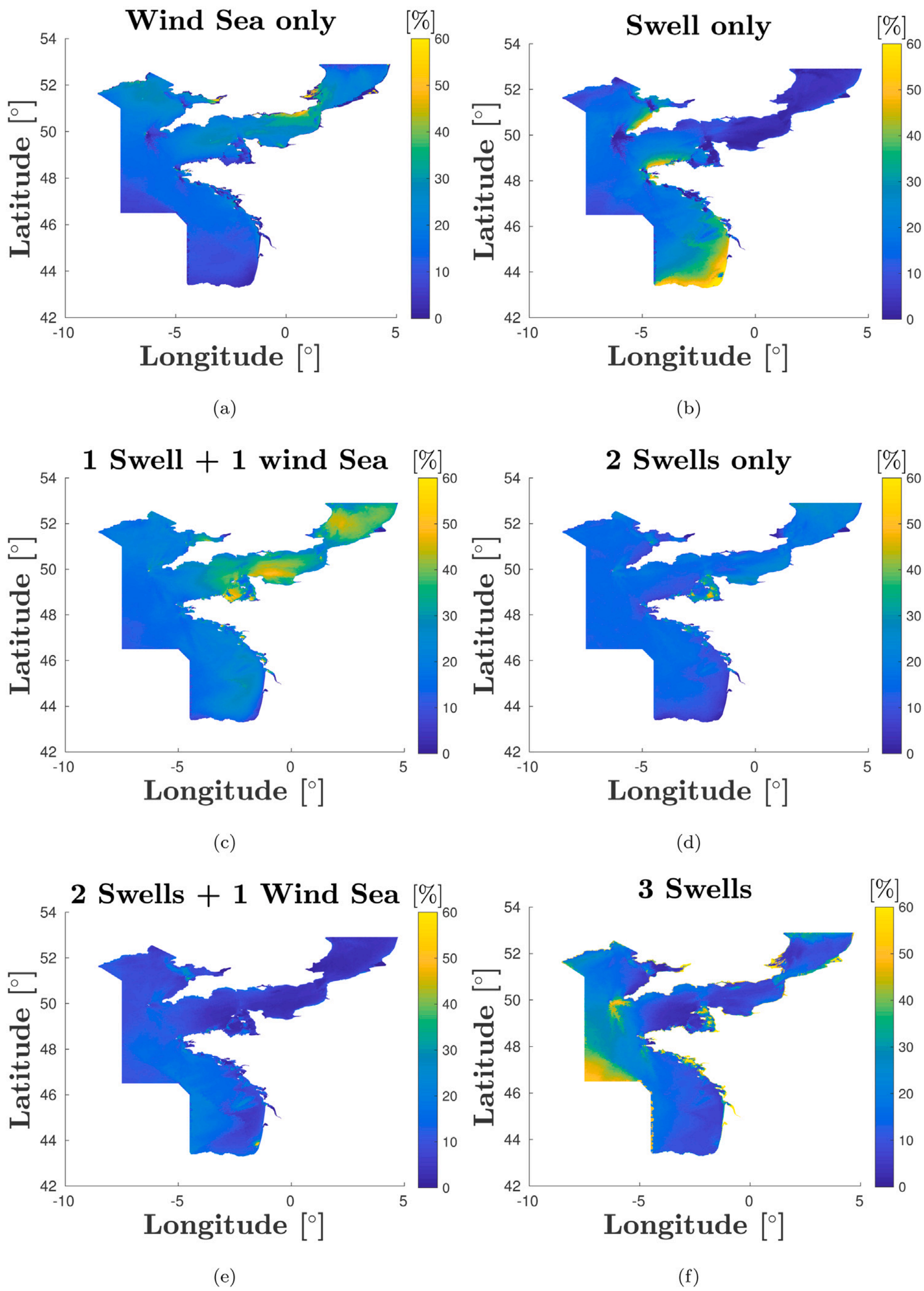


**Fig. 4.** Spatial distribution of occurrence statistics of wave systems.

**Table 1**
Name, coordinates, depth and percentage [%] contribution of the partitioning of key-points used for the analysis.

| Name | Coordinates [Lat-Lon] | Depth [m] | SP I | SP II | **Tot. Unimod.** | SP III | SP IV | SP V | SP VI | **Tot. Multimod.** |
|---|---|---|---|---|---|---|---|---|---|---|
| Pt 1 | 51.3°N, 6.5°W | 110.1 | 26.55 | 11.37 | **37.92** | 20.07 | 16.55 | 6.82 | 18.64 | **62.08** |
| Pt 2 | 49.0°N, 6.2°W | 124.0 | 12.11 | 10.53 | **22.64** | 16.47 | 15.03 | 11.51 | 34.35 | **77.36** |
| Pt 3 | 45.5°N, 3.0°W | 138.9 | 11.38 | 20.82 | **32.20** | 18.84 | 14.29 | 19.57 | 15.10 | **67.80** |
| Pt 4 | 44.0°N, 2.5°W | 839.5 | 11.34 | 37.36 | **48.70** | 23.52 | 9.97 | 9.94 | 7.87 | **51.30** |
| Pt 5 | 49.8°N, 2.5°W | 88.1 | 24.24 | 10.75 | **34.99** | 30.89 | 17.15 | 5.14 | 11.83 | **65.01** |
| Pt 6 | 52.5°N, 2.5°E | 49.9 | 23.94 | 7.57 | **31.51** | 34.72 | 17.56 | 6.28 | 9.93 | **68.49** |
| Pt 7 | 51.5°N, 8.0°W | 67.7 | 15.39 | 6.64 | **22.03** | 18.71 | 15.69 | 10.47 | 33.10 | **77.97** |
| Pt 8 | 50.0°N, 5.0°W | 73.7 | 15.92 | 9.32 | **25.24** | 26.24 | 17.71 | 11.27 | 19.54 | **74.76** |
| Pt 9 | 50.5°N, 3.0°W | 42.6 | 21.76 | 5.60 | **27.36** | 26.80 | 21.48 | 7.06 | 17.30 | **72.64** |
| Pt 10 | 50.5°N, 3.5°W | 63.4 | 33.32 | 22.35 | **55.67** | 11.96 | 4.02 | 19.63 | 8.72 | **44.33** |
| Pt 11 | 47.5°N, 3.0°W | 52.9 | 12.89 | 5.60 | **18.49** | 31.76 | 27.66 | 6.64 | 15.45 | **81.51** |
| Pt 12 | 50.5°N, 1.0°W | 24.9 | 30.29 | 3.48 | **33.77** | 42.07 | 13.81 | 3.27 | 7.08 | **66.23** |

et al.). Systems with three simultaneous swells are frequently observed, particularly in the western Bay of Biscay (Fig. 4(f)), as well as around the island and in some coastal areas. In summary, the North Celtic Sea appears to be marked by frequent occurrences of pure wind sea conditions, in contrast to the Western Celtic Sea, which is more frequently affected by swell systems. Similarly, unimodal conditions (swell only) and multimodal conditions (2 swells + 1 wind sea) characterize the southern and central Bay of Biscay, respectively. Another distinction emerges between the English Channel, especially its entrance, and the North Sea, each affected by distinct swell regimes. Further emphasizing the spatial division proposed in Sartini et al. (2018). Coastal areas of the Bay of Biscay and the South English Channel frequently exhibit systems with three swells.

### 3.2. Sub-regions and representative points

Following a comprehensive analysis of full-wave directional spectra and the occurrence statistics of wave systems, six points are chosen as representative indicators of the primary spectral systems identified in the area. These points serve to characterize the average conditions of the defined sub-regions (Fig. 5(a)). To examine the impact of local bathymetry, six additional points (i.e. Pt 7 to 12) have been identified as shown in Figs. 5(b) and 5(c). Additionally, points 10, 11, and 12 are also used to assess the influence of the tide, given their locations on relatively high tidal surge gradients. The coordinates and water depth for each of the selected locations are detailed in Table 1.

### 3.3. Spatial and inter-annual variability

Additional considerations on the spatial and inter-annual variability of spectral centroids in monthly directional spectra have been included to enhance the overall wave climate assessment in the study area. The outcomes, portraying the seasonal dispersion of centroids, are presented in Fig. 6.

There is a noticeable trend where seasonal centroids relative to Pt 1 consistently move along a common radial axis centred around the South-western direction. The only exception is January, which positions farther south, extending towards lower frequencies (higher periods) in March and throughout the winter season. Points Pt 2 and Pt 3 show similar patterns, displaying a greater dispersion around the western sector. Lower frequencies are observed in autumn and winter, with centroids moving in proximity to the South-West and North-West directions during winter and aligning around the West in summer. Similarly, Pt 4 centroids shift towards lower frequencies in winter along a common radial axis centred on the North-West. In January, the centre of mass moves further North. Pt 5 exhibits intermediate behaviour, aligning along the South-West axis and shifting radially between summer and winter, with centres positioned further South in December and January. Pt 6 shows higher dispersion, with centroids located in the North-West during spring, summer, and autumn. In winter, they shift towards the South-West, reaching the highest frequencies. The analysis of spatial distribution for Pt 7, 8, and 9 centroids reveals a consistent pattern across all three locations (Fig. 6): the centres exhibit radial movement in the South-West direction, with values associated with winter positioned at lower frequencies. The shallower nature of Pt 9 is reflected in the characteristic high frequency waves (short period) that reach this location after undergoing severe refraction process that pushes the direction towards south. Pt 10 centroids show the prevailing winterly nature of the location mainly characterized by wind-sea affected by the steep tidal surge gradient. The analysis of the centroids belonging to Pt 11 location highlights the dominant oceanic wave climate. The directions are mainly aligned with the main oceanic fetch, no directional variation is present both for high and low frequencies, with the latter mainly concentrated during the winter period. Pt 12 is the shallowest of the selected points. The waves that reach this location have been largely affected by the interaction with the bathymetry.

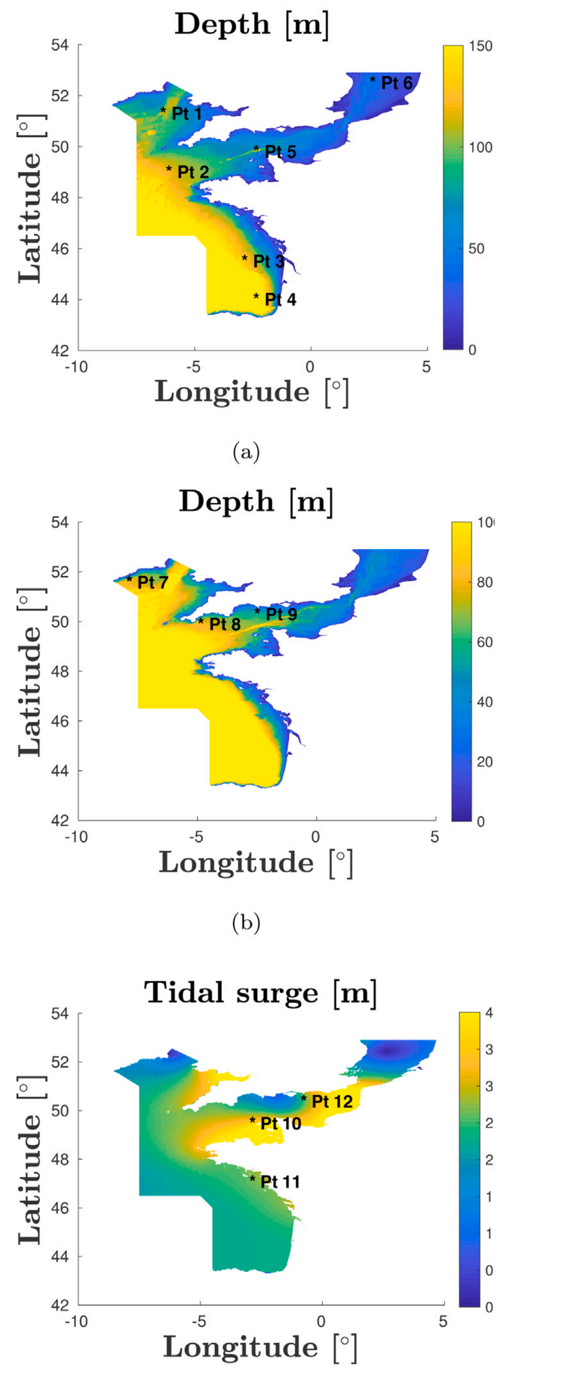


**Fig. 5.** Map of: 5(a) points selected for defining the spectral climatology types; 5(b) locations used for evaluating influence of bathymetry and 5(c) the tide effect.

The natural directional dispersion is limited due to a severe refraction process that aligns both sea wind and swells coming from the English channel. No significant variation can be detected among the different seasons. As outlined by Maisondieu et al. (2013) (Maisondieu and Le Boulluec, 2016), Fig. 7 illustrates the frequency distribution of the relative angles between wind sea and swell directions. This analysis aims to discern the occurrence frequency of hazardous crossing sea conditions.

At Pt 1, the most frequent crossed seas (approximately 60%) exhibit relative angles of 50–70° and 110–130° (Fig. 7(a)). At Pt 2, a significant

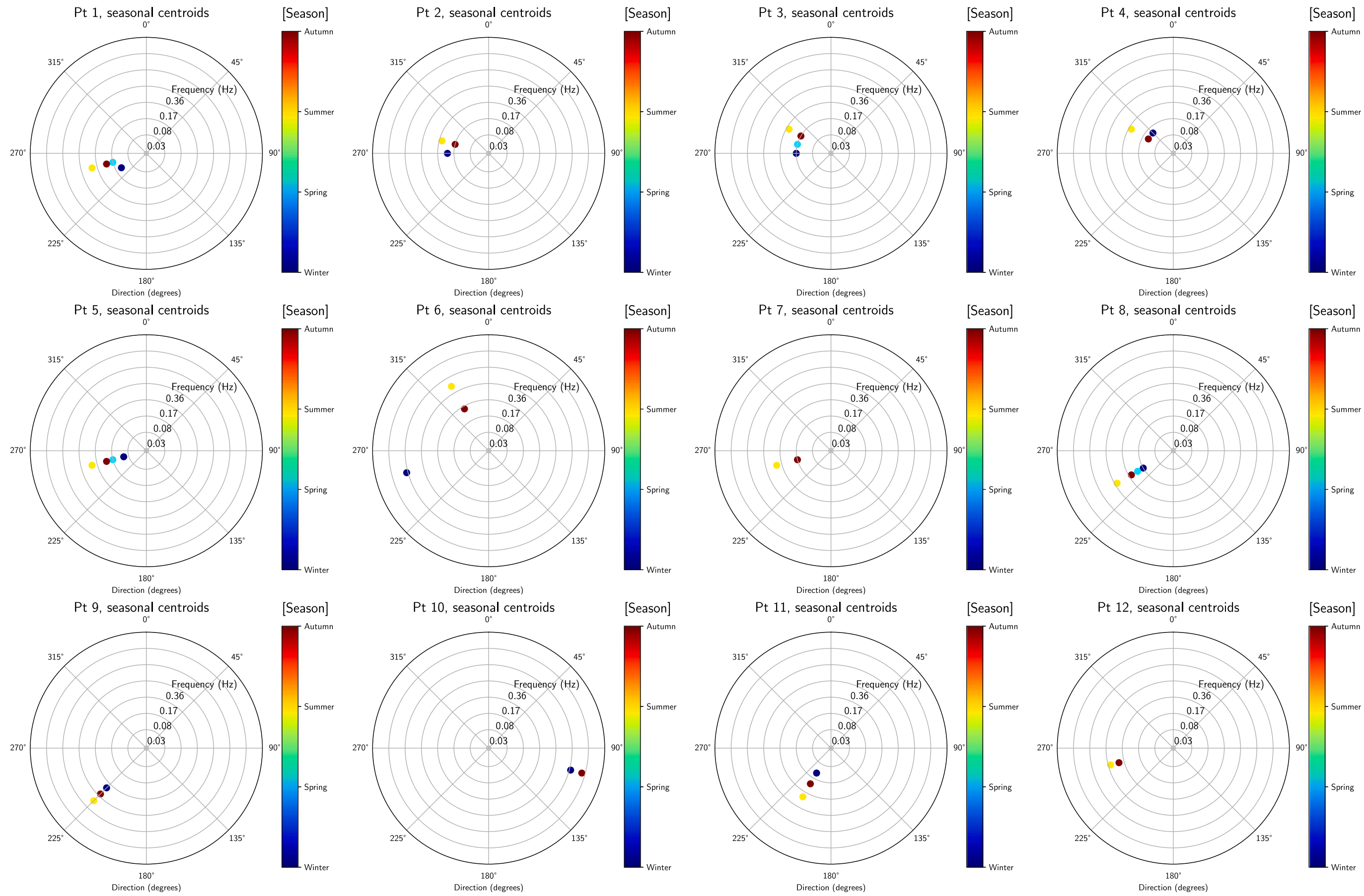


**Fig. 6.** Position variability of seasonal spectra centroids for all the locations.

portion (approximately 40%) is confined within the range of 70–100° (Fig. 7(b)). Points Pt 3 and Pt 4 both show the highest frequencies (approximately 50%) within a range of about 50°, specifically 60–90° and 50–80°, respectively in Figs. 7(c) and 7(d). For Pt 5, occurrences are located in two narrower sectors covering about 50% of the time 60–80° and 100–120°, Fig. 7(e). Pt 6 displays a greater dispersion around 60–120° as shown in Fig. 7(f). At Pt 7, the distribution of angular differences indicates that the most frequent occurrence of crossed seas happens within a range of 30° in two main sectors for about 50% of the time, 40–70° and 110–130° as presented in Fig. 7(g). In contrast, Pt 8 and Pt 9 display more intricate distributions, with three and four main classes, respectively in Figs. 7(h) and 7(i), covering about 50% of occurrences. Frequently crossed seas cover directions around 140° at Pt 8, creating the most hazardous conditions for shipping. At Pt 10, the most frequent (approximately 40%) crossing sea relative angle range is 40–60°, reflecting the limits imposed by the English Channel's west-most entrance, no additional crossing sea can be identified, see Fig. 7(j). Pt 11 consistently exhibits a narrow relative angle sector, ranging from 150–160°, for approximately 15% of the time. Additionally, less hazardous conditions are observed for 10% of the time, with a characteristic value falling within the range of 60–70°. In contrast, Pt 12 is characterized by a persistent crossing sea condition, accounting for approximately 55% of the time. This condition spans a range of relative angles between 70 and 110°, emphasizing the area's unique nature influenced by both the English Channel and North Sea wave climates.

### 3.4. Spectral climatology type

To evaluate the efficacy of employing an unstructured grid in conjunction with an appropriate wave model to accurately capture sea-state features characterized by the overlapping of multimodal seas on various scales, the directional wave spectra for Pt 1, Pt 2, Pt 5, and Pt 6 have been retrieved from the available 30-year NOAA wave hindcast climatology database.

Fig. 8 reports the wave energy directional density spectra for locations Pt1, Pt2, Pt5 and Pt6.

The average wave energy directional density spectra provided by the HOMERE database over the entire period of simulations are reported in Fig. 9.

The challenges encountered by a large-scale wave model, such as the NOAA model, become apparent when addressing sub-scale wave systems, like those influencing the study area. These sub-scale wave systems are, on the contrary, properly captured within the HOMERE database, as depicted in Figs. 9(a), 9(b), 9(e), and 9(f). This comparison reveals that the current uniform-resolution wave modelling approaches commonly employed in Earth system models may not adequately represent wave climates across various scales, from global to coastal regions. Additionally, these approaches may encounter difficulty in properly depicting both multimodal seas and directional spreading.

Given the complex and diverse nature of the wave climate in the study region, the peak period bivariate joint frequency distribution, proposed in Fig. 10, is adopted to capture the complexity of physical phenomena defining specific wave climate patterns. Each wave system is assumed to be independent in this analysis hence the bivariate joint

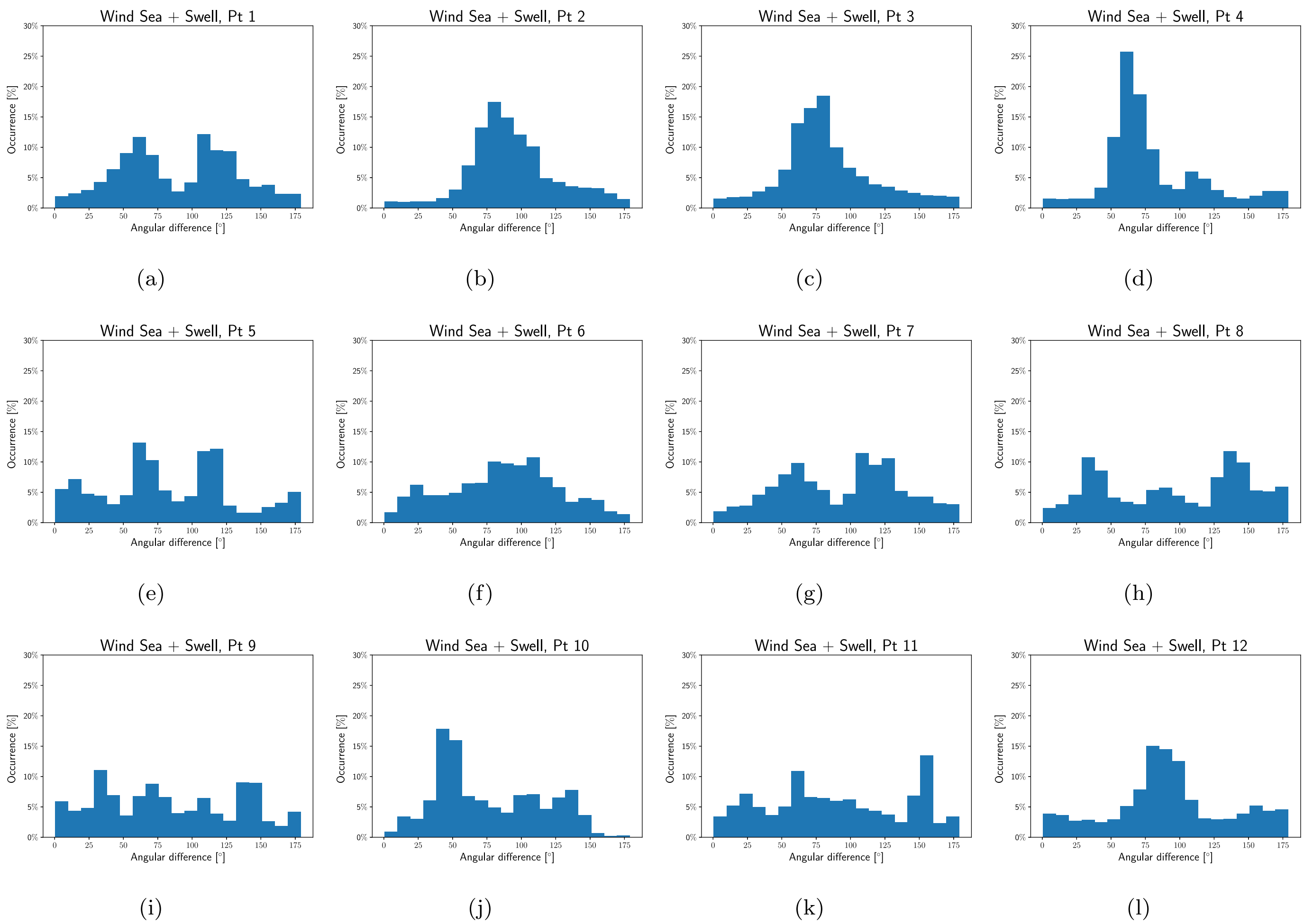


**Fig. 7.** Angular difference between wind seas and swells for all the locations.

frequency distributions are established by aggregating pairs of global parameters from all relevant wave systems within each partition, and the resulting normalized joint occurrences are then evaluated.

The main finding of the study is presented in Fig. 11 revealing that in more sheltered areas, seas predominantly exist in unimodal states. Conversely, in more open areas, multimodal states are prevalent, with wind seas gaining importance in regions characterized by shorter fetches. In nearshore and complex areas such as the English Channel, refraction emerges as a crucial factor contributing to the development of multimodal conditions. The following main climate systems, referred to as "Spectral Climatology" types, are presented based on their relative spectral partitioning assessments, serving as a summary of the entire wave climate for the study area.

### 3.4.1. *Spectral climatology type I, Area I*

The region represented by Pt 1 in Fig. 5(a) captures wave systems affecting the North Celtic Sea. The analysis indicates that Area I is characterized by a directional spread from the North-West to the South-East, covering a sector of approximately 180°. Notably, higher energy levels originate from the South-West, peaking during the winter season, with maximum values recorded in January. The energy levels gradually increase from October to January, followed by a significant decrease starting in March. Analysis of the peak period bivariate joint frequency distributions in Fig. 10(a) reveals that pure wind sea conditions predominantly impact South-West directions, with more intense events centred around 240°N. Multimodal sea states, particularly systems featuring the three swells, are observed in the South-West (240–250°N), South (180–190°N), and North-East (~ 30°N). This is evident through the significant contribution of swell seas, highlighted by the red clusters in the two main South-West sectors, along with minor events originating from the North-East. Multi-modal sea conditions dominate, constituting more than 60%, as depicted in Fig. 11(a). Detailed percentages for each partitioning type are provided in Table 1. Notably, the contribution from the first swell is significant, aligning closely with wind sea conditions, representing 20% of the total. Similarly, combinations of three swells contribute 18%. Such a climatology type can be associated with meteorological events coming from the West affecting the area at a meso-scale together with steady processes from the West/North-West active on a basin scale, responsible for swell events, as well described by the first swell system. In summary, "Spectral Climatology type I" is characterized by a 180° spread directional spectrum with prevailing energetic sectors in South-West; multimodal conditions are significant (62%) with the greatest contributions given respectively by a superimposition of wind seas and one swell and three swell systems, while unimodal sea-states are dominated by pure wind sea fraction (26%).

### 3.4.2. *Spectral climatology type II, Area II*

The directional spectrum for location Pt 2 is reported in Fig. 9(b). Energies are spread within a sector of ~225° with higher energies coming from West direction mainly in January, while in spring and summer, more intense events arise from the North-West. Another important contribution comes from North-East. Wind sea conditions are registered on West (270° N), South-East(150° N) and North-East (70° N) directions; swell systems are found to affect different directions overlapped with wind sea-states, with longest waves coming from West (250–300° N),

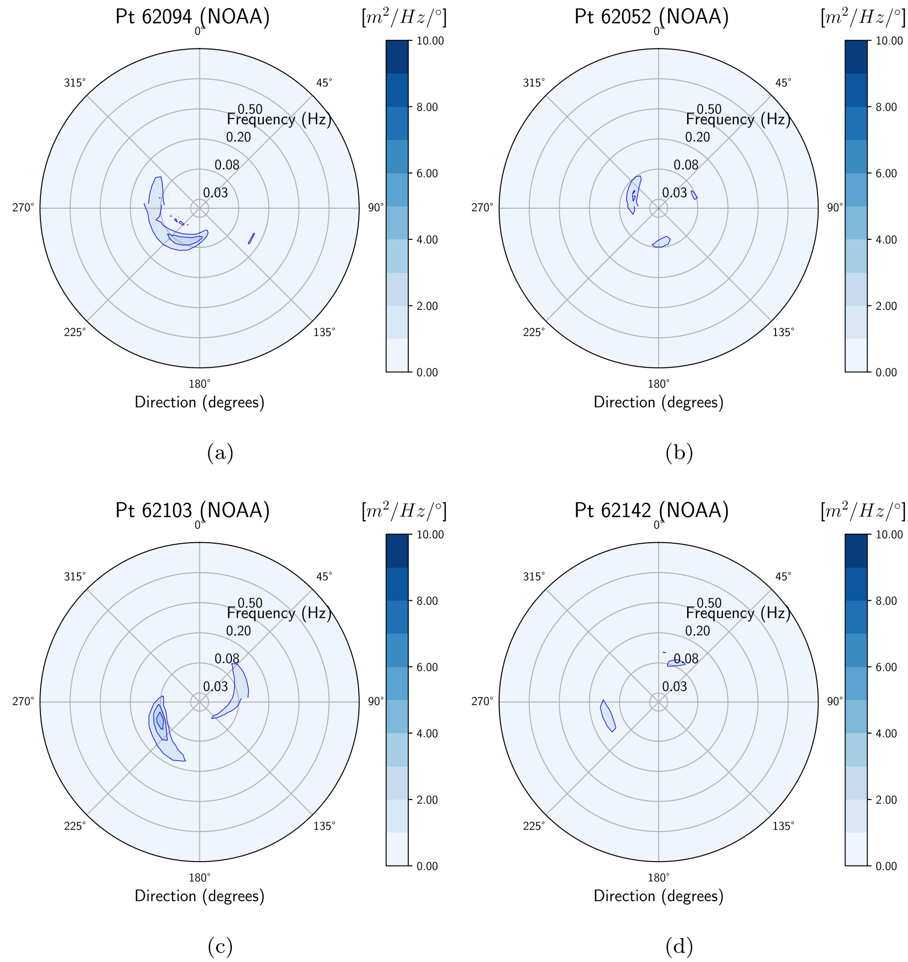


**Fig. 8.** NOAA wave energy directional density spectra for locations Pt1, Pt2, Pt5 and Pt6.

from South and North (Fig. 10(b)). The complex patterns observed in this area signify a pronounced multimodal nature, accounting for over 70%, with the most substantial contributions originating from the combination of three swells (34%), as emphasized in Fig. 11(a). Unimodal sea states are characterized by comparable occurrences of wind sea and single swell and are presented in Table 1. Overall this area exhibits a large fraction of multimodal conditions with a prevalence of combined swell seas.

This type of spectral climatology is associated with greater exposure to meteorological events active on a meso-scale coming from the West, responsible for the full development of wind sea conditions together with superposed swell seas due to North large-scale perturbations. Furthermore, the refraction effects performed by the Brittany coast trigger the onset of processes active on a sub-scale responsible for steady North-East events.

### 3.4.3. *Spectral climatology type III, Area III*

Location Pt 3 exhibits a widespread wave energy distribution spanning almost 360°, as illustrated in Fig. 9(c). The most intense energy levels are observed in the North-West direction, particularly in January and February. Wind sea conditions are found to be significant within a specific sector (250–300°N) and extend eastward, partially overlapping with swell systems. These wind sea conditions impact both the North-West sector (250–350°N) and the South-West region (∼ 220°N, Fig. 10(c)). The whole area is dominated by multimodal conditions (70%, Table 1) with the largest contribution given by the sea-state of two swell (19%), while unimodal seas are dominated by swell (20%) (Fig. 11(a)). "Spectral Climatology Type III" is marked by a highly scattered directional spectrum spread on almost 360°. Pure wind seas are generated by large scale perturbations coming from the West together with the concurrent development of significant North-West swell events also affecting the South-West. This spectral partition can be linked to the distinctive characteristics of the area, influenced by the bathymetry gradient, which contributes to the formation of crossed sea states.

### 3.4.4. *Spectral climatology type IV, Area IV*

Moving into the southern Celtic Sea, the directional spectra distinctly reveal a heightened influence from the North-West sector, extending across a span of 180° (Fig. 9(d)). This sector experiences peak energy levels during January and February. The region is impacted by wind sea conditions, affecting the direction of 250–350°N also crossing substantial swell systems (Fig. 10(d)). This overlapping translates into a balance between unimodal (48%) and multimodal (52%) conditions (Table 1), whose respective prevalence is given by swell sea-states (37%) and by wind sea with 1 swell (23%) (Fig. 11(a)). The "Spectral Climatology type IV" exhibits a 180° directional spectrum exposed to North-West, responsible for the development of stable swell sea conditions, as evidenced by Maisondieu (2017). More precisely, wind sea conditions are found to be about one-third of first swell system occurrences. Indeed, while SWH relative to the wind sea system are more spatially diversified within area III, and on average lower than values registered in the Celtic Sea, those related to system II are more uniform.

Overall, area IV located on the South Bay of Biscay seems to feel the refraction effect triggered by the coastline as well as the bathymetry

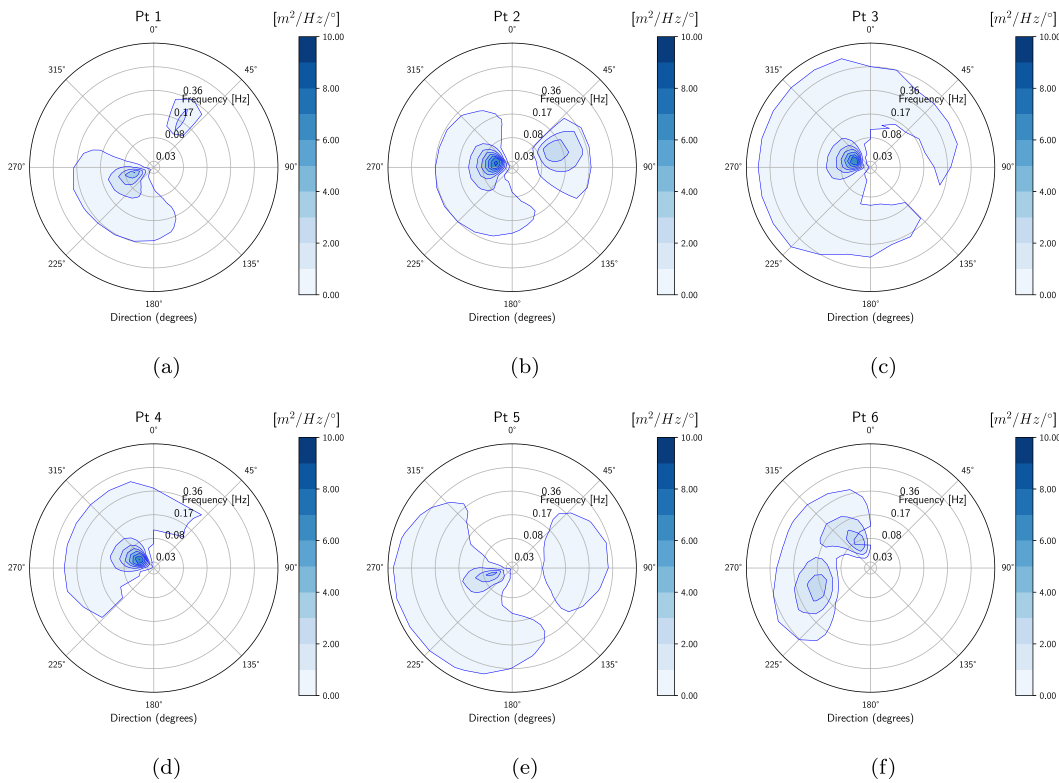


**Fig. 9.** Wave energy directional density spectra for location Pt 1 - Pt 6.

gradient in the proximity of the continental shelf on the development of marked swell sea-states, in addition to diffraction and protection effect induced by Galicia. Wind sea fraction in partition I remains significant and similar to previous areas while swell contribution reduces substantially.

#### 3.4.5. Spectral climatology type V, Area V

The directional spectra for Point Pt 5 are oriented towards the South-West, spanning 180° and exhibiting a double-peaked pattern in opposite directions (Fig. 9(e)). The maximum energy is characteristic of December and January with wind sea conditions primarily observed in the West (~ 250°N) and North-East (50–100°N) directions, overlapping with swell seas that also influence the South-West (Fig. 10(e)). Nevertheless, the percentage contribution of swell in unimodal conditions (35%, Table 1) turns out to be 10% (Fig. 11(a)); multimodal seas (65%) are prevalent and represented mainly by SP III (wind sea+1 swell, 30%, Table 1).

The regions bounded by the English Channel, where complex sea states arise from wind channelling and the substantial influence of tides collaborate to delineate "Spectral Climatology type V", are distinguished by a noteworthy presence of swell seas crossing with pure wind seas in the same direction and exhibiting double-peaked directional spectra. This phenomenon is also documented by Mason et al., highlighting the prevalence of bi-modal seas at locations exposed to Atlantic swells, which seldom propagate the entire length of the English Channel to the Straits of Dover.

#### 3.4.6. Spectral climatology type VI, Area VI

The North Sea area is marked by bimodal systems, as shown by directional spectra presented in Fig. 9(f) for location Pt 6. Bimodal seas are consistently present throughout the year, with peak intensities observed in December, January, and February. These bimodal conditions manifest in two primary directions – South-West and North-West – separated by approximately ~ 70°. The contribution of swells in unimodal seas decreases from 31% to 7% (Table 1). Multimodal conditions (31%) are predominantly influenced by SP III (35%), as illustrated in Fig. 11(a). The entire area is characterized by peculiar features of partitioning; indeed, while wind sea interests mainly the South-West (sector 200–250°N), swell seas are relevant to North-West (300–350°N) (Fig. 10(f)).

The marked behaviour of the area defines the "Spectral Climatology type VI" as a complex system, associated with wind events coming from the North-West active on a basin scale together with sub-scale processes triggered by the peculiar topography of the sub-area. Along the Dutch coast, the most intense storms come from the North whereas those more frequent originate from the English Channel.

### 3.5. Influence of bathymetry

To assess the impact of bathymetry on energy spectra, we conducted additional analyses focusing on specific sub-areas. We selected six further points: Points 7, 8, and 9, situated near steep bathymetric gradients in coastal regions (Fig. 5(b)). In these areas, the depth undergoes rapid changes from a hundred metres to a few dozen metres. Additionally, three other points (Pt 10, 11, 12 in Fig. 5(c)) were chosen near steep tidal surge gradients, ensuring comparability with the subsequent section exploring the influence of tides.

Pt 7 shows a large exposure sector spread of more than 180° included between East and West directions (Fig. 12(a)). Higher energies and frequencies are reached in January and December; during spring and summer the spectrum is confined to the South-West. Prevailing conditions are multimodal seas (78%) mainly due to the presence of three swells (33%) (Fig. 11(b)), while the contribution given by swell system in unimodal conditions is low (6%) (Table 1). Statistical analyses of SWH concerning wind-driven seas indicate a predominant distribution in the South-West sector (200–250°N). Conversely, swell seas exert influence over a broader region extending to the West (up to 270°N) and also in the South directions. The distribution of peak periods further illustrates that swells are primarily concentrated at the

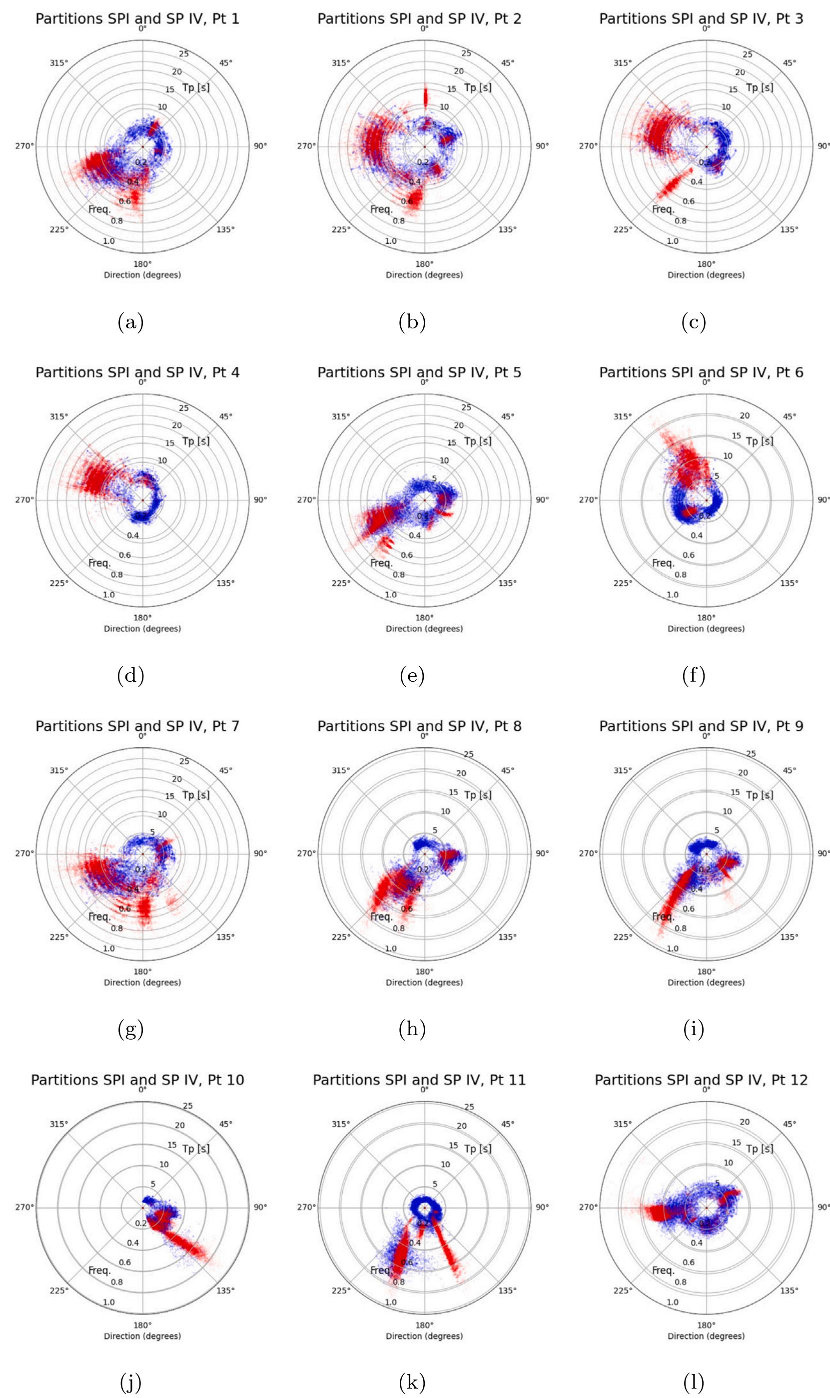


**Fig. 10.** Bivariate joint frequency distribution (normalized counts) of peak period in function of mean direction for the partitions SP I and IV and all the selected locations. In red: SP I, in blue: SP IV.

boundaries of the most energetic sector covered by the wind-driven sea (see Fig. 10(g)).

Location Pt 8 exhibits a directional spectrum resembling the preceding one, characterized by more energetic conditions in the South-West sector spanning over 180° of directional spreading. This spectrum displays higher frequencies and features a minor peak in the East direction (see Fig. 12(b)). The bimodal nature of this spectrum is observable from October to April, with the exception of November. The two peaks are approximately 130° apart. Multimodal conditions prevail, constituting 74% of the occurrences. The primary contributors are wind-driven sea and swell partition (26%), as depicted in Fig. 11(b), followed by the combination of three swells (19%). The percentage of swell fractions in unimodal seas remains small at 9% (refer to Table 1). Notably, the partitioned SWH are distributed over the same sectors, specifically 200–250°N and around 100°N. Furthermore, the distribution of peak periods highlights that swell seas are more confined to the boundaries of the most energetic sector (see Fig. 10(h)).

Similar to Pt 8, the directional spectra at Point 9 exhibit a 180° spread, mainly covering the South-West direction, especially for the more energetic values (see Fig. 12(c)). A double peak is noticeable from October to April, excluding November. In unimodal conditions (21%), where one dominant peak exists, swell contribution is minor (5%), with wind-driven sea fraction dominating (Fig. 11(b)). Multimodal conditions prevail (72%), primarily contributed by SP III (27%), IV

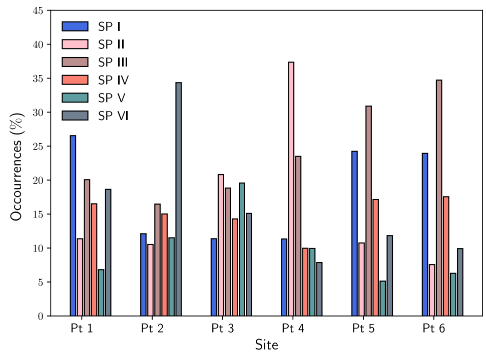


(a)

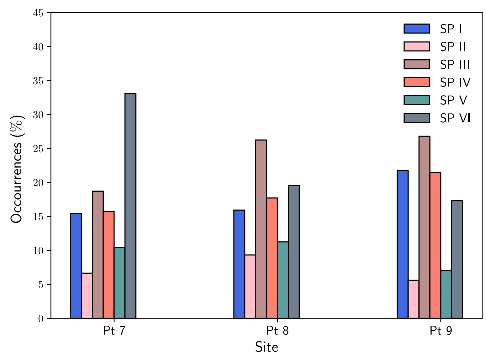


(b)

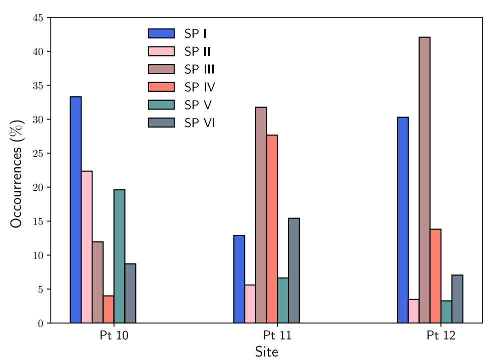


(c)

**Fig. 11.** Normalized percentage occurrences of wave systems at points 1–6 11(a), 7–9 11(b) and 9–12 11(c).

(21%), and VI (17%) (refer to Table 1). This complexity is reflected in the distribution of partitioned significant wave heights, which, on average, cover three main sectors (around 100°, 150°, and 220°N). The distribution of peak periods, given by partition II, reveals the presence of two distinct narrow peaks, mirroring the patterns observed in the previous case (see Fig. 10(i)).

Point 10 exhibits a directional spectrum oriented towards the South-East, with energy peaks occurring predominantly between October and April. Unimodal conditions dominate (55%), with a prevalent presence of wind seas (33%). Although swells still contribute significantly (22%), as illustrated in Fig. 11(c), multimodal seas are characterized by the presence of three swell systems (19%) (see Table 1). As a result, the partitioned significant wave heights of wind seas are primarily distributed over the 80–150°N sector, with more frequent occurrences around 100°N and 120°N, superimposed on swell seas. Additionally, swell events are more concentrated in the 120°N direction, evident in the narrow peak periods distribution, while the wind sea system exhibits more uniform conditions (refer to Fig. 10(j)).

At Point 11, directional spectra demonstrate a bimodal pattern, primarily centred on a narrow sector pointing to the South-West (Fig. 12(e)). This spread covers approximately 90°, while an additional peak in the South-West direction emerges in December, accompanied by a direction shift towards the West in the latter part of the year. Multimodal conditions dominate significantly (81%), with SP III (31%) and IV (27%) being the predominant contributors (see Fig. 11(c)). The contribution of swell in unimodal seas remains low at 5% (see Table 1). Wind-driven SWH are uniformly distributed within the primary sector, with higher occurrence frequencies in the vicinity of about 200°N. In contrast, the distribution related to swells reveals that SWH are organized into two main classes, centred around 200°N and 150°N. Similarly, peak periods exhibit a behaviour featuring two narrow peaks for swell seas (see Fig. 10(k)). Pt 12 properly describes the bimodal nature of the area, as demonstrated by directional spectra shows in Fig. 12(f). The presence of a double peak can be observed in the opposite direction with respect to the main provenance sector for most of the year reflecting both the larger amount of wave energy coming from the English Channel and the refracted Northern Sea waves that reach this location. Again, multimodal conditions are dominant (66%) with a prevalence of SP III (42%) (Fig. 11(c)); unimodal seas are governed by wind sea partition (39%) while swell contribution is negligible (3%) ( Table 1). SWH distribution of wind seas and swell partitions reveal a similar behaviour, with the main classes centred respectively on 250°N, 170°N and 50°N directions; peak periods distributions reveal a similar arrangement with swell systems more narrow in the proximity of opposite directions (Fig. 10(l)).

In summary, bathymetry seems to provide a non-negligible effect on directional spectra shape within the northern area of study, enhancing a bimodal distribution. It is well-known that the transformation of swell from open ocean to coastal areas is strongly affected by propagation over shelf features which can imply spatial variations on wave heights (Munk and Traylor, 1947) mainly due to wave refraction as the primary mechanism while friction, diffraction, and other processes can be of secondary importance only. There are only few studies of swell evolution (Hasselmann and Olbers, 1973; Young and Gorman, 1995; Ardhuin et al., 2001). In Herbers et al. (2000), for instance, the transformation of swell across continental shelf is examined showing a significant attenuation of high-energy swell across the shelf performed by bottom boundary layer processes, not predicted by refraction models. The analysed directional spectra exhibit a notable broadening as waves propagate depth gradients, aligning with the expectations outlined in Bragg scattering theory for random waves interacting with irregular seafloor topography (Ardhuin and Herbers, 2002). This observed phenomenon contrasts with the predictions of refraction theory, which anticipates a narrowing effect (Ardhuin et al., 2003). This observation holds true for numerous locations situated near distinctive bathymetric features, such as abrupt depth changes and steep gradients. Remarkably, in comparison to previous areas where the separation of peak periods exhibited a more continuous trend, the influence of bathymetry in these locations appears to accentuate a significant discontinuity. This is evident in the partitioned quantities aligned with the corresponding mean directions. Moreover, the impact of bathymetry renders the contribution of swells in unimodal conditions negligible. The percentage fraction of multimodal sea states surpasses the 70%.

### 3.6. Influence of tide

The influence of tidal forces emerges as a significant factor in directional spectra assessment, particularly in regions characterized by robust tidal currents, as highlighted by Ardhuin et al. (2012). Incorporating tidal forcing into wave models has proven beneficial for refining

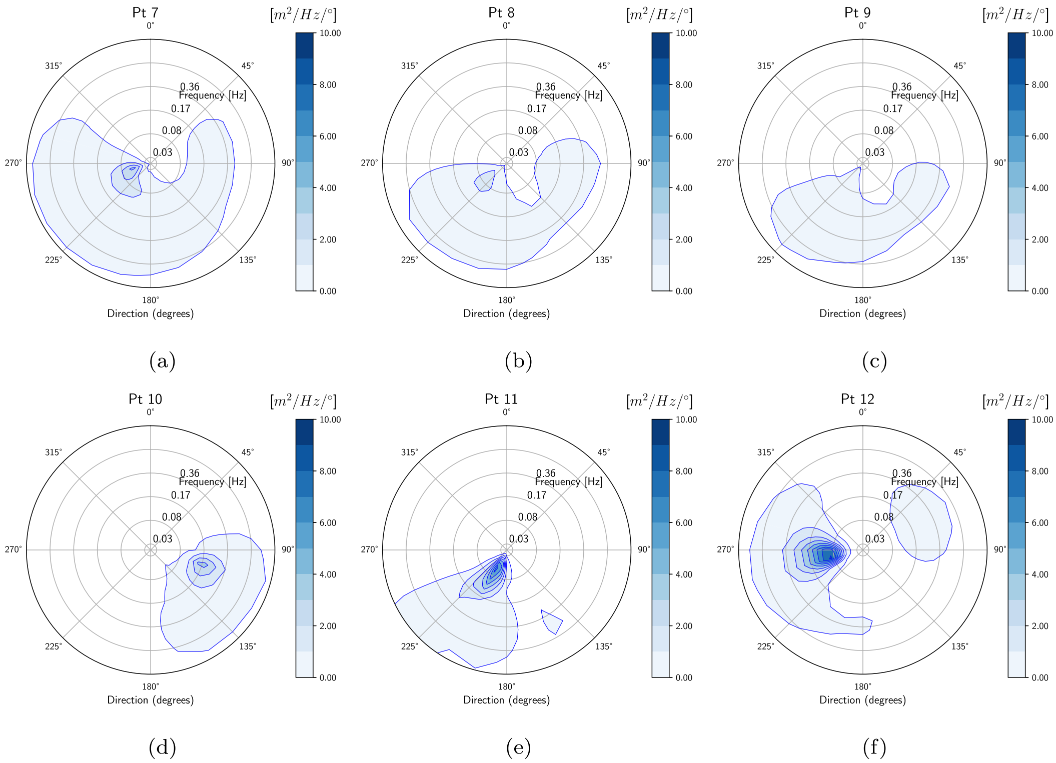


**Fig. 12.** Wave energy directional spectra for location Pt 7 - Pt 12.

the description of refraction induced by currents, resulting in fluctuations in significant wave height. Key contributors to these variations include current-induced refraction, the occurrence of waves breaking on opposing currents and the transfer of energy among the spectral frequencies (Guillou, 2017). In particular, points situated close to tidal surge gradients appear to be shielded by the formation of well-defined unimodal swell seas. In this work, the impact of tides on directional spectra is investigated via spectral analysis conducted at specific points strategically chosen close to steep tidal surge gradients, where the most significant interaction between tidal-induced hydrodynamics and the wave field is anticipated (see Fig. 5(c)). For the sake of brevity, only three points corresponding to the three high tidal surge gradients and covering the central English channel Pt 10, the Atlantic area Pt 11 and the shallow English coastal waters Pt 12, are discussed here as representative cases.

Point 10 stands out as it predominantly experiences the impact of the wind channelling system in the area. For other locations, the contribution of crossed-sea states is noteworthy. Peak periods exhibit a distinct bimodal distribution, and tide effects manifest in the development of bimodal seas with spectra spreading in opposite directions. The influence of tide on wave spectra was examined during both ebb and flood tide conditions. The results reveal that the influence of tide on wave spectra is almost negligible at location Pt 10 during both ebb and flood conditions, with directional spectrum oriented towards the South-East, with a spread of approximately 90° due to the pronounced refraction caused by the tidal gradient. Effect that is more pronounced at higher frequencies (see Fig. 12(d)). This is supported by Fig. 13, where the flood only affects the width of the wave spectrum; the overall peak direction remains constant, aligning with the behaviour described in Fig. 12(d).

For locations Pt 11 and Pt 12, instead, while the ebb phase is characterized by uniform wave conditions, the flood condition stands out for the presence of the mentioned bimodal distributions, especially for location Pt11, where the directional spectrum is normally characterized by a bimodal behaviour here is enhanced by the presence of two broaden peaks spread of 60–90°. The presence of double peaks in opposite directions observed at location Pt12 in Fig. 12(f) is not present anymore during the flood, even though multimodal conditions have been established compared to the ebb phase. Fig. 13(f) illustrates the directional spectra at the shallowest (i.e. Pt 12) among the three investigated points, also the point that experiences the most significant interaction between tidal currents and the wave field. The difference observed between ebb and flood conditions primarily arises from the distinct alignment of wave and current directions. During flood conditions, the current aligns closely with the wave propagation direction, resulting in an increase in wavelength. As a result, this gives rise to shallower water wave conditions compared to scenarios without current, facilitating a more substantial transfer of energy to both super- and sub-harmonics. The centroids of the three energy peaks depicted in Fig. 13(f) are approximately multiples or sub-multiples of each other. Another interesting behaviour pertains to the directional shift in these energy clusters. The longest waves refract earlier, causing their direction at Point 12 to be more perpendicular to the coastline during flood conditions. In contrast, the shorter waves, influenced by the seafloor later, reach Pt 12 location more aligned with the axis of the English Channel.

### 3.7. Long term trend

With the increasing importance and attention to the climate change effects on the oceanographic variables, the analysis of wave climate long-term variation has been widely investigated recently and in the last couple of decades due to its high engineering relevance (De Leo et al., 2020; Haigh et al., 2010; Lowe et al., 2010; Reguero et al., 2019). Such variations can be largely relevant for coastal and offshore areas, as they may, in turn, modify the equilibrium of the coastline (Zhang et al., 2004), the type of coastal protection interventions e.g. from hard to soft engineering (Morris et al., 2020), the flood hazard and vulnerability management (Nicholls and Klein, 2006), the marine ecosystem (Harley et al., 2006) and the offshore and coastal economic activities (Raby et al., 2019), in particular in an areas densely populated and economically active as the one under investigation.

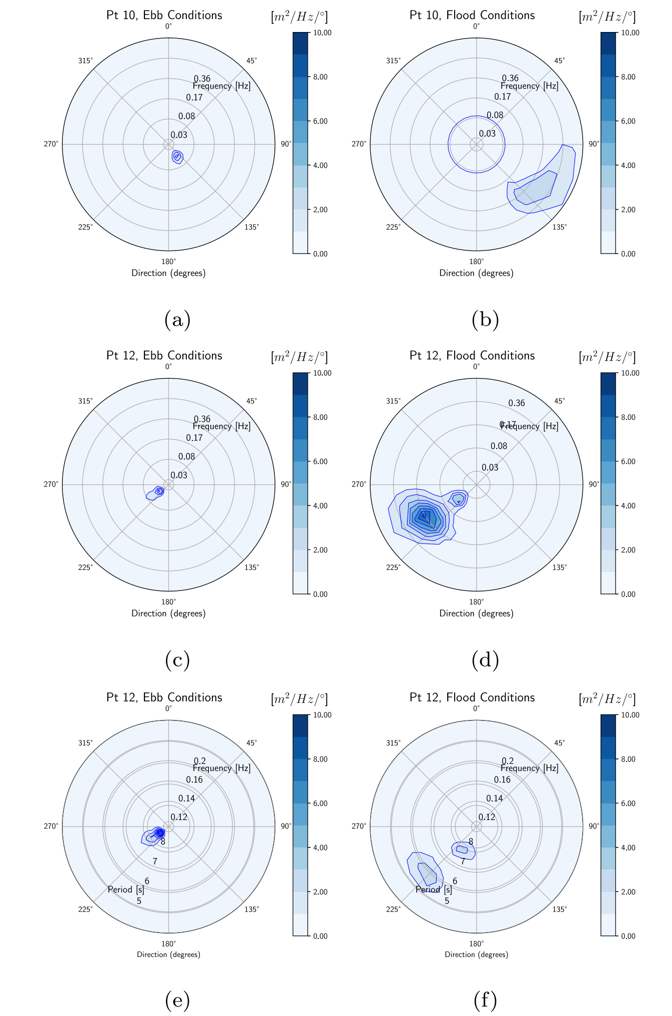


**Fig. 13.** Wave energy directional density spectra during the ebb and flood phase for locations Pt10, Pt11 and Pt12.

A commonly applied method for trend detection is the non-parametric Mann–Kendall test (MN) (Mann, 1945) based on the sample rank correlation. However, MN is rather sensitive to data seasonality and data serial dependence (or autocorrelation) resulting in misinterpretation of the trend test results and increasing the chance of significant answer even in the absence of a real trend (Cox and Stuart, 1955). Although the issues related to the seasonality were successfully addressed by Hirsch and Slack (1984) through the seasonal Mann–Kendall test, the induced bias due to the data autocorrelation was only resolved by Hamed and Ramachandra Rao (1998) by proposing the Modified Mann–Kendall test (MMK).

Thus, to provide an overall characterization of the area, the long term trend analysis is performed for the 12 points under investigation and for both $H_s$ and $T_p$.

Therefore, due to the highly seasonal nature of the wave climate, in this work the use of a deseasonalisation pre-process – aimed to remove the overshadowing effect of seasonality – is adopted in combination with the application of the MMK to the residuals resulting from the time series decomposition presented in (3), as proposed by Findley et al. (1998),

$$H_s = H_{s,t} \cdot H_{s,s} \cdot H_{s,i} \tag{3}$$

where $H_{s,t}$, $H_{s,s}$ and $H_{s,i}$ represent the trend, the seasonal and the stochastic components, respectively. Among the four available time series decompositions methods, i.e. additive, multiplicative and log-additive and pseudo-additive, the multiplicative one is selected as the most appropriate because of the (i) positive values of the wave parameters, (ii) the non-constant size of the seasonal oscillations and (iii) the negligible number of small values (i.e. close to zero) in the analysed time series, (Findley et al., 1998).

Hence the recorded SWH monthly maxima time series (the same applies for $T_p$) is decomposed into three components, the trend component ($H_{s,t}$), the seasonal component ($H_{s,s}$) and the stochastic (also called irregular or residual) component ($H_{s,i}$). The deseasonalisation procedure is subdivided into five steps of increasing accuracy for the estimation of the monthly maxima seasonal component and seasonally adjusted time series. The first step is aimed at preliminary identifying the linear trend through the application of a 13-term symmetric moving average. The second step focuses on the identification of the seasonal component using a seasonal 5-term moving average applied to the detrended data. The third step aims to improve the linear trend estimation by applying a 13-term Henderson filter (Kenny and Durbin, 1982) to the previously seasonally adjusted data while later (fourth step) a 7-term seasonal moving average is applied to the newly detrended data to obtain an improved estimation of the seasonal component. Finally (fifth step) the seasonally adjusted data is obtained by dividing the original data with the later improved estimation of the seasonal component.

Therefore the stochastic component obtained by the last operation (blue line in Fig. 14 and Fig. 15), combining both the linear trend and the stochastic component, is used for the long-term trend detection through the MMK. The main results of the deseasonalisation procedure are presented in Fig. 14 and Fig. 15 for the monthly maxima $H_s$ and $T_p$ respectively. For the sake of visual purpose each panel of Fig. 15 presents an additional box where both detrended and seasonal adjusted results are shown.

The application of the deseasonalisation procedure is not only effective in highlighting the stochastic part of the data, e.g. Pt8 and Pt9 in Fig. 14 clearly show the peak related to the heavy storm in 2014 that caused major damage all along the southern UK coast but is also rather effective to reduce the data serial correlation as shown in Fig. 16 for monthly maxima $H_s$ (Pt7) and for monthly maxima $T_p$ (Pt12). The magnitude and significance of linear trends are investigated for the seasonal corrected hourly $H_s$ and $T_p$ data for the 12 representative points. The MMK – and in particular the calculated $p$-value – is used to assess the statistical significance of the monotonic trend (e.g. Masina et al. (2022)), while the linear slope is evaluated through Sen's method (Kenny and Durbin, 1982). The distinction between the two adopted metrics is mainly that the MMK $p$-value allows to discriminate of the significance of the monotonic trend, so that, if the obtained value is close to 0 either a positive or negative monotonic trend characterizes the analysed data, i.e. the null hypothesis; on the contrary, values close to 1 indicate that the null hypothesis should be rejected (De Leo et al., 2021). Additionally, another statistic obtained on running the Mann–Kendall test is Kendall's tau-b, which is a measure of the correlation and therefore measures the strength of the relationship between the two variables, i.e. either SWH or Tp and time. The tau-b statistic, unlike tau-a, makes adjustments for ties. Values of tau-b range from −1 (100% negative correlation) to +1 (100% positive correlation), a value of zero indicates the absence of correlation. On the other hand, Sen's slope does not provide any information about the statistical significance but provides the magnitude of the slope calculated as the median trend values within the data and the 95% confidence interval under the hypothesis of normally distributed values. A summary of the results for the 12 investigated points is presented in Table 2 for both $H_s$ and $T_p$. The detected Sen's slope values are summarized in the fourth column where the values between squared brackets indicate the 95% confidence interval.

The selected 12 locations are representative of the variety of the different conditions and they aim to cover the entire analysed domain. A consistent negative trend is detected across the entire domain with

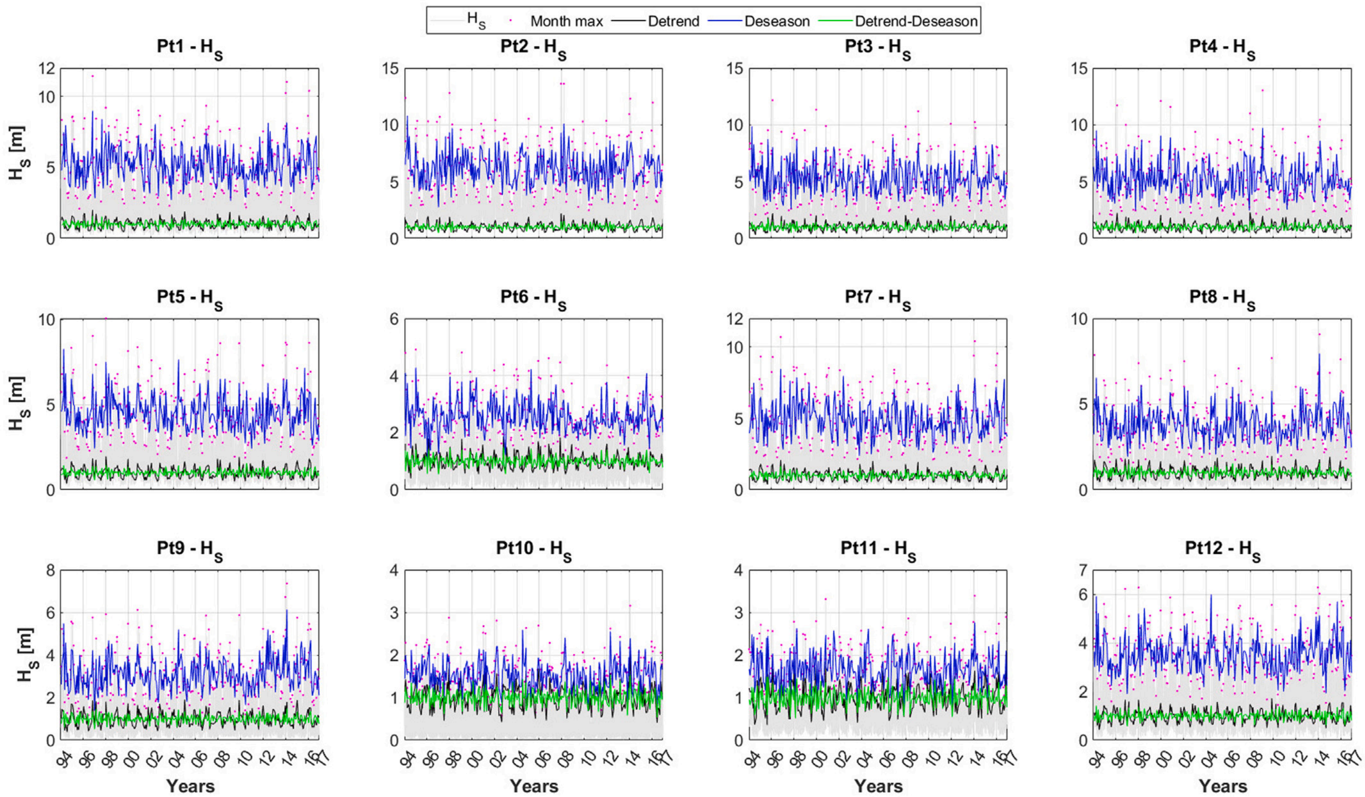


**Fig. 14.** Results of the multiplicative decomposition applied to the original $H_s$ data presented in grey, monthly maximum in pink, detrended data in black, deseasonalized data in blue and both deseasonalized and detrended data in green.

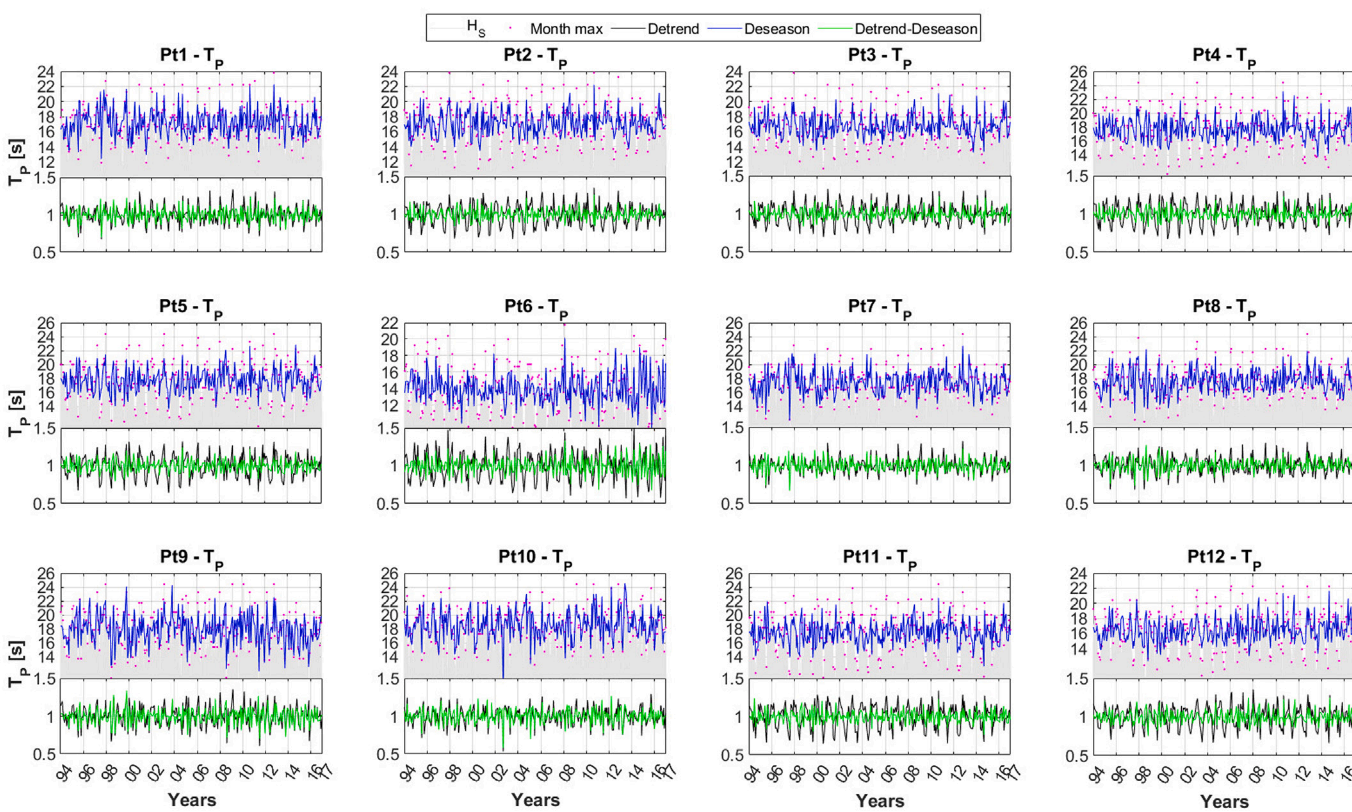


**Fig. 15.** Results of the multiplicative decomposition applied to the original $T_p$ data presented in grey, monthly maximum in pink, detrended data in black, deseasonalized data in blue and both deseasonalized and detrended data in green.

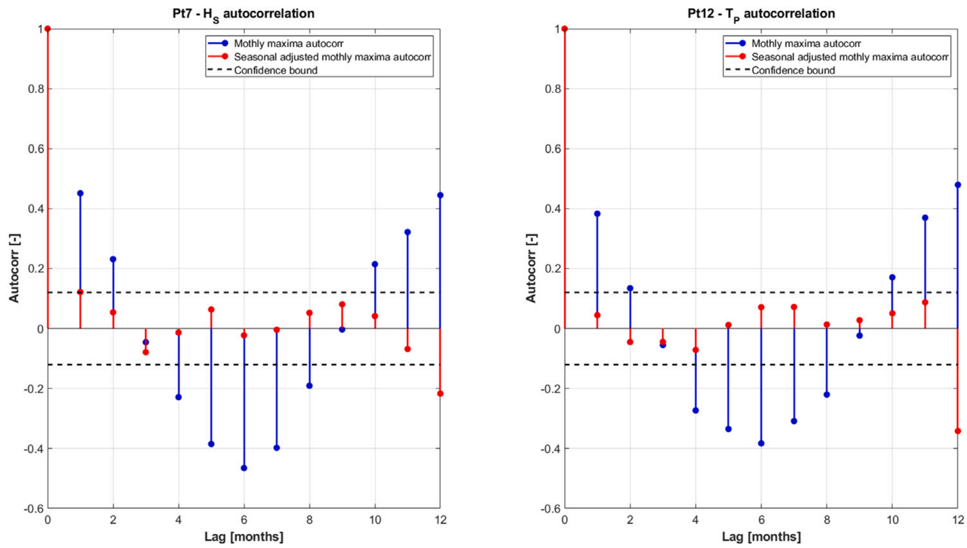


**Fig. 16.** Autocorrelation function monthly maxima and seasonal adjusted monthly maxima.

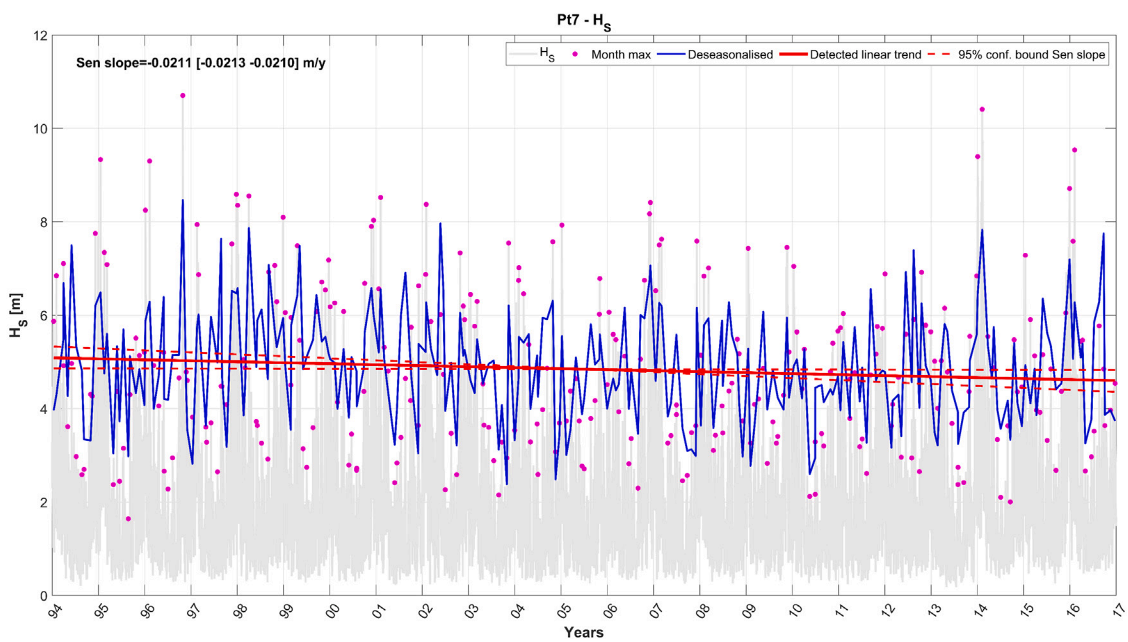


**Fig. 17.** Point 7, $H_s$ time series, seasonally corrected data and detected Sen's slope.

**Table 2**
$H_s$ and $T_p$ trend metrics for the 12 investigated points.

| | $H_s$ and $T_p$ trend | | | |
|---|---|---|---|---|
| Point | $H_s$-MMK p-value | $H_s$-tau-b | $T_p$-MMK p-value | $T_p$-tau-b |
| Pt 1 | 0.189 | −0.054 | 0.984 | −0.001 |
| Pt 2 | 0.228 | −0.050 | 0.573 | 0.023 |
| Pt 3 | 0.182 | −0.055 | 0.941 | 0.003 |
| Pt 4 | 0.164 | −0.057 | 0.817 | −0.010 |
| Pt 5 | 0.129 | −0.063 | 0.354 | 0.038 |
| Pt 6 | 0.054 | −0.079 | 0.126 | −0.063 |
| Pt 7 | 0.039 | −0.085 | 0.992 | 0.000 |
| Pt 8 | 0.915 | 0.004 | 0.458 | 0.031 |
| Pt 9 | 0.259 | 0.047 | 0.243 | −0.048 |
| Pt 10 | 0.361 | −0.038 | 0.400 | 0.035 |
| Pt 11 | 0.607 | −0.021 | 0.375 | 0.036 |
| Pt 12 | 0.429 | 0.033 | 0.031 | 0.089 |

regards to $H_s$, with Sen's slope values ranging between −0.02 m/y (Point 7, 17) to few (or none) millimetres per year. As expected, a generalized negative correlation between the *p*-value, the absolute value of the Sen's slopes and tau-b values, is observed. Therefore is questionable the statistical significance of the smallest values of the detected Sen's slope. Indeed, only Point 7 shows a *p*-value close to zero (<0.05) indicating a strong statistical significance of the detected trend, also confirmed by the large negative tau-b value. On the other hand, Point 6, shows a rather small *p*-value and large negative tau-b value but the detected Sen's slope, i.e. 8 mm/year, is one of the smallest among the identified ones. The latter can be reasonably correlated with the shallow water nature of this point (14.2 m) which imposes an upper limit for the wave height growth. Significant negative Sen's slope values around −0.015 m/year are also detected for Points 1, 2, 3, 4 and 5, however, the identified large p-values indicate weak empirical evidence to accept the null hypothesis. No significant trends are found for Points 8, 9, 10, 11, and 12, all of them characterized by rather large p-values

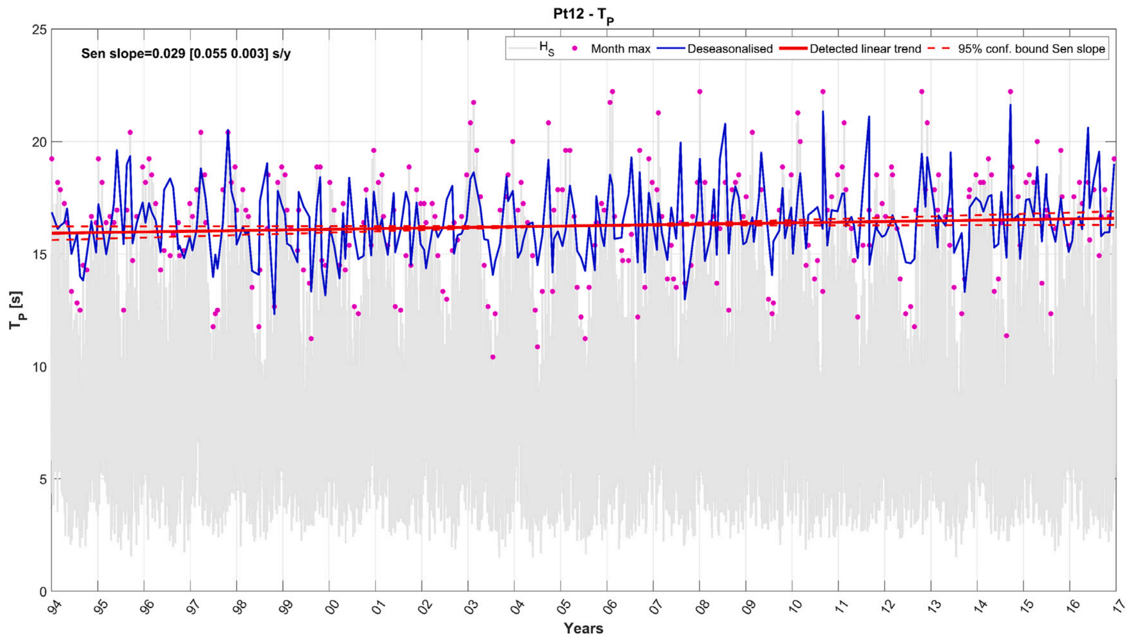


**Fig. 18.** Point 12, $T_p$ time series, seasonally corrected data and detected Sen's slope.

(i.e. > 0.2) and small absolute values of the Sen's slopes, i.e. in the order of few millimetres per year.

With regards to $T_p$, a consistent positive trend is detected across 6 out of 12 analysed points, with rather small positive Sen's slope values ranging between 0.03 s/y (Point 12, Fig. 18) to 0.01 s/y. Negative Sen's slope values are detected for Point 6 and 9, while the remaining investigated points, i.e. Points 1, 3, 4, and 7, do not show any significant trend. Also in this case, a generalized negative correlation between the *p*-value and the absolute values of the Sen's slopes and tau-b is observed. Only Point 12 shows a *p*-value close to zero (<0.05) indicating strong empirical evidence to accept the null hypothesis, i.e. the presence of a monotonic trend in the data. Accordingly, also tau-b assumes the largest value, confirming the presence of an upward trend that is further corroborated by the detected Sen's slope equal to 0.03 s/y, the largest among the identified ones. On the contrary, Points 6 and 9, show negative Sen's slope and tau-b values, however, the calculated p-values (i.e. 0.126 and 0.243 respectively) do show rather weak evidence to ascertain the presence of a trend. Points 2, 5, 8, 10 and 11, all present positive Sen's slope values between 0.02 and 0.01 s/y, however, the identified p-values do not confirm the significance of the trend. The remaining points, i.e. 1, 3, 4 and 7 do not show any significant trend slope that is further corroborated by the large p-values and the small tau-b values.

Despite both CFSR (Stopa and Cheung, 2014; Aarnes et al., 2015) products might experience the issue of spurious trends induced by the data assimilation procedure, the investigated area shows rather homogeneous spatial behaviour, therefore we hypothesize that the results among the investigated points are comparable and can offer a comprehensive picture of the relative importance within the area. Thus, it can be concluded that no generalized significant trends are detected within the investigated spatial domain for the variables at stake, i.e. $H_s$ and $T_p$. Moreover, assuming a MMK significance level equal to 5%, only Point 7 shows a downward $H_s$ trend (−0.021 m/y), while only Point 12 shows a $T_p$ upward trend (0.03 s/y).

## 4. Conclusions

This study endeavours to scrutinize the spectral climatology of the French Atlantic Ocean coastal region by employing a 23-year wave spectral hindcast database. The primary objective is to delineate the predominant "Spectral Climatology Types" influencing the investigated area. Through meticulous evaluations of directional spectra and spectral partitions, six distinct "Spectral Climatology Types" are identified and comprehensively described.

In particular, areas confined in the northern Celtic Sea (e.g. Pt 1) are characterized by a 180°-spread (North-West/South-East) directional spectrum with a prevalence of multimodal conditions resulting from the presence of wind seas superimposed to one swell and from systems of three swells. Wind sea fraction contribution is significant.

Western Celtic Sea (e.g. Pt 2) is affected by higher energies as a result of a full exposure to West/North-West wind events together with a full exposure to North-East which translates into a reduction of unimodal conditions on behalf of the development of multimodal seas, in particular of three swell systems. Refraction effects dur to the coast are fairly clear as demonstrated by the marked presence of North-East events.

Points located within the South Celtic Sea (e.g. Pt 3) exhibit a highly scattered directional spectrum covering the whole set of directions and marked by the presence of crossed sea states, especially in proximity of slope bathymetry, with major contribution given by the combination of swell seas, mainly due to the combination of large-scale perturbations coming from North-West together with the effect performed by bathymetry gradient. On the contrary, areas confined in the southern Bay of Biscay (e.g. Pt 4) share a narrower North-West directional spectra and both unimodal and multimodal sea conditions are found in equal measure. The presence of fully developed swell system is marked and mainly triggered by the refraction effect performed by the coastline and bathymetry gradient.

The English Channel (e.g. Pt 5) is marked by complex sea systems due to both effects of wind channelling and tide influence which contribute to the development of swell crossing pure wind seas in similar directions and by a double-peaked directional spectrum. Similarly, the area of the North Sea (e.g. Pt 6) exhibits marked bimodal features within the whole year with a double-peaks directional spectrum, as a result of wind events coming from North-West together with processes active on a sub-scale triggered by the peculiar topography. Wind sea fraction reaches its maximum value; swell contribution in unimodal seas proves to be not significant.

The examination of bathymetric effects underscores its pivotal role in shaping the wave climate. Specifically, distinctive conditions such as abrupt depth changes and steep gradients exert a significant influence on the directional spectra, particularly in the northern basin. These conditions amplify the broadening of spectra shapes, leading to the development of bimodal spectra and a heightened discontinuity in partitioned quantities, such as peak periods.

The wave refraction induced by tidal currents amplifies the emergence of bimodal spectra, characterized by peak spread occurring in opposite directions. This phenomenon is accompanied by the highest percentage of swell contribution in multimodal seas as confirmed by the relative angular directions.

An in-depth examination of the position of directional spectra centres of mass is also provided. The findings indicate a shift from South-West to North-West as one moves from the North Celtic Sea to the South Bay of Biscay. This shift is particularly noticeable for lower frequency, extending from winter to early spring. The centres of mass in the English Channel are predominantly located in the South-West, whereas the North Sea exhibits a greater dispersion of centroids in both North-West and South-West directions.

The establishment of "Spectral Climatology Types" for the French Atlantic Ocean, derived from spectral partition analysis, has significantly enhanced our understanding of the wave climate in this pivotal region. This knowledge holds particular relevance at the core of significant activities, including the maritime design of systems like EMR (Energies Marines Renouvelables) and ETM (Energie Thermique des Mers) in both coastal and cyclonic areas.

## CRediT authorship contribution statement

**Ludovica Sartini:** Writing – review & editing, Writing – original draft. **Alessandro Antonini:** Validation, Supervision, Data curation.

## Declaration of competing interest

The authors declare that they have no known competing financial interests or personal relationships that could have appeared to influence the work reported in this paper.

## Data availability

Data will be made available on request.

## Acknowledgements

Wave data sets for this paper are available at https://forms.ifremer.fr/lops-oc/marc-homere/. L.Sartini acknowledges M.Prevosto and C.Maisondieu for the interesting discussion on wave dynamics.

## References

Aarnes, O.J., Abdalla, S., Bidlot, J.-R., Breivik, Øyvind, 2015. Marine wind and wave height trends at different era-interim forecast ranges. J. Clim. 28 (2), 819–837. http://dx.doi.org/10.1175/JCLI-D-14-00470.1.

Ailliot, P., Maisondieu, C., Monbet, V., 2013. Dynamical partitioning of directional ocean wave spectra. Probab. Eng. Mech. 33, 95–102.

Anon, 2019. Survivability assessment of fastnet lighthouse. Coast. Eng. 150, 18–38.

Anon, 2021a. Layout optimization of heaving wave energy converters linear arrays in front of a vertical wall. Renew. Energy 179, 189–203.

Anon, 2021b. Shifting wave energy perceptions: The case for wave energy converter (wec) feasibility at milder resources. Renew. Energy 170, 1143–1155.

Antonini, A., Archetti, R., Lamberti, A., 2017. Wave simulation for the design of an innovative quay wall: The case of Vloré harbour. Nat. Hazards Earth Syst. Sci. 17 (1), 127–142. http://dx.doi.org/10.5194/nhess-17-127-2017.

Ardhuin, F., Chapron, B., Collard, F., 2009. Observation of swell dissipation across oceans. Geophys. Res. Lett. 36 (6).

Ardhuin, F., Herbers, T.H.C., 2002. Bragg scattering of random surface gravity waves by irregular seabed topography. J. Fluid Mech. 451, 1–33. http://dx.doi.org/10.1017/S0022112001006218.

Ardhuin, F., Herbers, T.H.C., O'Reilly, W.C., 2001. A hybrid Eulerian–Lagrangian model for spectral wave evolution with application to bottom friction on the continental shelf. J. Phys. Oceanogr. 31 (6), 1498–1516.

Ardhuin, F., O'Reilly, W.C., Herbers, T.H.C., Jessen, P.F., 2003. Swell transformation across the continental shelf. Part I: Attenuation and directional broadening. J. Phys. Oceanogr. 33 (9), 1921–1939. http://dx.doi.org/10.1175/1520-0485(2003)033<1921:STATCS>2.0.CO;2.

Ardhuin, F., Roland, A., 2012. Coastal wave reflection, directional spread, and seismoacoustic noise sources. J. Geophys. Res.: Oceans 117 (C11).

Boudière, E., Maisondieu, C., Ardhuin, F., Accensi, M., Pineau-Guillou, L., Lepesqueur, J., 2013. A suitable metocean hindcast database for the design of marine energy converters. Int. J. Mar. Energy 3–4, e40–e52.

Chen, Z., Zhang, L., Zhao, C., Chen, X., Zhong, J., 2015. A practical method of extracting wind sea and swell from directional wave spectrum. J. Atmos. Ocean. Technol. 32 (11), 2147–2159.

Cox, D.R., Stuart, A., 1955. Some quick sign tests for trend in location and dispersion. Biometrika 42 (1/2), 80–95.

De Leo, F., Besio, G., Briganti, R., Vanem, E., 2021. Non-stationary extreme value analysis of sea states based on linear trends, analysis of annual maxima series of significant wave height and peak period in the Mediterranean sea. Coast. Eng. 167, 103896. http://dx.doi.org/10.1016/j.coastaleng.2021.103896, URL https://www.sciencedirect.com/science/article/pii/S0378383921000569.

De Leo, F., De Leo, A., Besio, G., Briganti, R., 2020. Detection and quantification of trends in time series of significant wave heights: An application in the Mediterranean sea. Ocean Eng. 202, 107155. http://dx.doi.org/10.1016/j.oceaneng.2020.107155.

Devaliere, E., Hanson, J., Luettich, R., 2009. Spatial tracking of numerical wave model output using a spiral search algorithm. In: 2009 WRI World Congress on Computer Science and Information Engineering, Vol. 2. CSIE 2009, pp. 404–408.

Espejo, A., Camus, P., Losada, I.J., Méndez, F.J., 2014. Spectral ocean wave climate variability based on atmospheric circulation patterns. J. Phys. Oceanogr. 44 (8), 2139–2152. http://dx.doi.org/10.1175/JPO-D-13-0276.1.

Ewans, K.C., Bitner-Gregersen, E.M., Soares, C.G., 2004. Estimation of wind-sea and swell components in a bimodal sea state. J. Offshore Mech. Arct. Eng. 128 (4), 265–270.

Findley, D.F., Monsell, B.C., Bell, W.R., Otto, M.C., Chen, B.-C., 1998. New capabilities and methods of the x-12-arima seasonal-adjustment program. J. Bus. Econom. Statist. 16 (2), 127–152.

Gerling, T.W., 1992. Partitioning sequences and arrays of directional ocean wave spectra into component wave systems. J. Atmos. Ocean. Technol. 9 (4), 444–458.

Haigh, I., Nicholls, R., Wells, N., 2010. Assessing changes in extreme sea levels: Application to the English channel, 1900–2006. Cont. Shelf Res. 30 (9), 1042–1055. http://dx.doi.org/10.1016/j.csr.2010.02.002.

Hamed, K.H., Ramachandra Rao, A., 1998. A modified Mann-Kendall trend test for autocorrelated data. J. Hydrol. 204 (1), 182–196. http://dx.doi.org/10.1016/S0022-1694(97)00125-X.

Hanson, J.L., Jensen, R.E., 2004. Wave system diagnostics for numerical wave models. In: 8th International Workshop on Wave Hindcasting and Forecasting, JCOMM Tech., vol. 29.

Hanson, J.L., Phillips, O.M., 1999. Wind sea growth and dissipation in the open ocean. J. Phys. Oceanogr. 29 (8), 1633–1648.

Hanson, J.L., Phillips, O.M., 2001. Automated analysis of ocean surface directional wave spectra. J. Atmos. Ocean. Technol. 18 (2), 277–293.

Harley, C.D.G., Randall Hughes, A., Hultgren, K.M., Miner, B.G., Sorte, C.J.B., Thornber, C.S., Rodriguez, L.F., Tomanek, L., Williams, S.L., 2006. The impacts of climate change in coastal marine systems. Ecol. Lett. 9 (2), 228–241.

Hasselmann, S., Brüning, C., Hasselmann, K., Heimbach, P., 1996. An improved algorithm for the retrieval of ocean wave spectra from synthetic aperture radar image spectra. J. Geophys. Res.: Oceans 101 (C7), 16615–16629.

Hasselmann, K., Olbers, D., 1973. Measurements of wind-wave growth and swell decay during the joint North Sea wave project (JONSWAP). Ergänzung zur Deut. Hydrogr. Z. Reihe A 12 (8), 1–95.

Herbers, T.H.C., Hendrickson, E.J., O'Reilly, W.C., 2000. Propagation of swell across a wide continental shelf. J. Geophys. Res.: Oceans 105 (C8), 19729–19737.

Hirsch, R.M., Slack, J.R., 1984. A nonparametric trend test for seasonal data with serial dependence. Water Resour. Res. 20 (6), 727–732.

Jonathan, P., Ewans, K., Forristall, G., 2008. Statistical estimation of extreme ocean environments: The requirement for modelling directionality and other covariate effects. Ocean Eng. 35 (11), 1211–1225.

Kenny, P.B., Durbin, J., 1982. Local trend estimation and seasonal adjustment of economic and social time series. J. R. Stat. Soc. Ser. A (General) 145 (1), 1–41.

Komen, G.J., Hasselmann, S., Hasselmann, K., 1984. On the existence of a fully developed wind-sea spectrum. J. Phys. Oceanogr. 14 (8), 1271–1285. http://dx.doi.org/10.1175/1520-0485(1984)014<1271:OTEOAF>2.0.CO;2.

Kpogo-Nuwoklo, K.A., Ailliot, P., Olagnon, M., Guédé, Z., Arnault, S., 2015. Improvement ocean wave spectra estimation using the temporal structure of wave systems. Coast. Eng. 96, 81–91.

Lazure, P., Dumas, F., 2008. An external–internal mode coupling for a 3d hydrodynamical model for applications at regional scale (Mars). Adv. Water Resour. 31 (2), 233–250.

Lowe, J.A., Woodworth, P.L., Knutson, T.R., McDonald, R.E., McInnes, K.L., Woth, K., von Storch, H., Wolf, J., Swail, V.R., Bernier, N.B., Gulev, S.K., Horsburgh, K., Unnikrishnan, A.S., Hunter, J.R., Weisse, R., 2010. Past and future changes in extreme sea levels and waves.

Maisondieu, C., 2017. Statistical characterization of complex sea-states in the bay of biscay for the design of marine structures. Houille Blanche (6), 40–48.

Maisondieu, C., Le Boulluec, M., 2016. Benefits of using a spectral hindcast database for wave power extraction assessment. Int. J. Ocean Clim. Syst. 7 (3), 83–87.

Mann, H.B., 1945. Nonparametric tests against trend. Econometrica 13 (3), 245–259, URL http://www.jstor.org/stable/1907187.

Masina, M., D'Ayala, D., Antonini, A., 2022. Variations in monthly maximum gust speed at St Mary's, Isles of Scilly (UK). Earth Space Sci. 9 (11), e2022EA002380.

Mason, T., Bradbury, A., Poate, T., Newman, R., Nearshore wave climate of the english channel – evidence for bi-modal seas. In: Coastal Engineering 2008. pp. 605–616.

Morris, R., Boxshall, A., Swearer, S., 2020. Climate-resilient coasts require diverse defence solutions. Nature Clim. Change 10, 1–3. http://dx.doi.org/10.1038/s41558-020-0798-9.

Munk, W.H., Traylor, M.A., 1947. Refraction of ocean waves: A process linking underwater topography to beach erosion. J. Geol. 55 (1), 1–26.

Nicholls, R., Klein, R., 2006. Climate change and coastal management on Europe's coast. pp. 199–226.

Olagnon, M., Kpogo-Nuwoklo, K.A., Guédé, Z., 2014. Statistical processing of West Africa wave directional spectra time-series into a climatology of swell events. J. Mar. Syst. 130, 101–108.

Polidoro, A., Pullen, T., Eade, J., Mason, T., Blanco, B., Wyncoll, D., 2018. Gravel beach profile response allowing for bimodal sea states. Proc. Inst. Civ. Eng. - Marit. Eng. 171 (4), 145–166. http://dx.doi.org/10.1680/jmaen.2018.11.

Portilla, J., Ocampo-Torres, F.J., Monbaliu, J., 2009. Spectral partitioning and identification of wind sea and swell. J. Atmos. Ocean. Technol. 26 (1), 107–122. http://dx.doi.org/10.1175/2008JTECHO609.1.

Portilla-Yandún, J., 2018. The global signature of ocean wave spectra. Geophys. Res. Lett. 45 (1), 267–276.

Portilla-Yandún, J., Salazar, A., Cavaleri, L., 2016. Climate patterns derived from ocean wave spectra. Geophys. Res. Lett. 43 (22), 11,736–11,743.

Raby, A.C., Antonini, A., Pappas, A., Dassanayake, D.T., Brownjohn, J.M.W., D'Ayala, D., 2019. Wolf rock lighthouse: Past developments and future survivability under wave loading. Phil. Trans. R. Soc. A 377 (2155), 20190027. http://dx.doi.org/10.1098/rsta.2019.0027.

Reguero, B., Losada, I., Méndez, F., 2019. A recent increase in global wave power as a consequence of oceanic warming. Nature Commun. 10 (1).

Saha, S., Moorthi, S., Pan, H.-L., Wu, X., Wang, J., Nadiga, S., Tripp, P., Kistler, R., Woollen, J., Behringer, D., Liu, H., Stokes, D., Grumbine, R., Gayno, G., Wang, J., Hou, Y.-T., Chuang, H.-Y., Juang, H.-M.H., Sela, J., Iredell, M., Treadon, R., Kleist, D., Van Delst, P., Keyser, D., Derber, J., Ek, M., Meng, J., Wei, H., Yang, R., Lord, S., Van Den Dool, H., Kumar, A., Wang, W., Long, C., Chelliah, M., Xue, Y., Huang, B., Schemm, J.-K., Ebisuzaki, W., Lin, R., Xie, P., Chen, M., Zhou, S., Higgins, W., Zou, C.-Z., Liu, Q., Chen, Y., Han, Y., Cucurull, L., Reynolds, R.W., Rutledge, G., Goldberg, M., 2010. The NCEP climate forecast system reanalysis. Bull. Am. Meteorol. Soc. 91 (8), 1015–1057.

Sanil Kumar, V., Singh, J., Pednekar, P., Gowthaman, R., 2011. Waves in the nearshore waters of Northern Arabian Sea during the summer monsoon. Ocean Eng. 38 (2), 382–388.

Sartini, L., Weiss, J., Prevosto, M., Bulteau, T., Rohmer, J., Maisondieu, C., 2018. Spatial analysis of extreme sea states affecting Atlantic France: A critical assessment of the rfa approach. Ocean Model. 130, 48–65.

Scipione, F., De Girolamo, P., Castellino, M., Pasquali, D., Celli, D., Di Risio, M., 2024. Reduced wave time series for long-term morphodynamic applications. Coast. Eng. 189, 104453. http://dx.doi.org/10.1016/j.coastaleng.2024.104453.

Stopa, J.E., Cheung, K.F., 2014. Intercomparison of wind and wave data from the ecmwf reanalysis interim and the ncep climate forecast system reanalysis. Ocean Model. 75, 65–83. http://dx.doi.org/10.1016/j.ocemod.2013.12.006.

Tracy, B., Devaliere, E., Hanson, J., Nicolini, T., Tolman, H., 2007. Wind sea and swell delineation for numerical wave modeling. In: Proceedings of 10th international workshop on wave hindcasting and forecasting and coastal hazard symposium, North Shore, Oahu, Hawaii, vol. 2007, pp. 11–16.

Vincent, L., Soille, P., 1991. Watersheds in digital spaces: An efficient algorithm based on immersion simulations. IEEE Trans. Pattern Anal. Mach. Intell. 13 (6), 583–598.

Voorrips, A.C., Makin, V.K., Hasselmann, S., 1997. Assimilation of wave spectra from pitch-and-roll buoys in a North Sea wave model. J. Geophys. Res.: Oceans 102 (C3), 5829–5849. http://dx.doi.org/10.1029/96JC03242.

Young, I.R., Gorman, R.M., 1995. Measurements of the evolution of ocean wave spectra due to bottom friction. J. Geophys. Res.: Oceans 100 (C6), 10987–11004.

Zhang, K., Douglas, B., Leatherman, S., 2004. Global warming and coastal erosion. Clim. Change 64, 41–58. http://dx.doi.org/10.1023/B:CLIM.0000024690.32682.48.